ISPRS Journal of Photogrammetry and Remote Sensing 204 (2023) 237–256

Contents lists available at ScienceDirect

ISPRS Journal of Photogrammetry and Remote Sensing

journal homepage: www.elsevier.com/locate/isprsjprs

Atmosphere-aware photoclinometry for pixel-wise 3D topographic mapping of Mars

Wai Chung Liu, Bo Wu *

Planetary Remote Sensing Laboratory, Department of Land Surveying & Geo-Informatics | Research Centre for Deep Space Explorations, The Hong Kong Polytechnic University, Hung Hom, Kowloon, Hong Kong, China

ARTICLE INFO

Keywords:
3D Mapping
Atmosphere-aware
Photoclinometry
Mars
HiRISE
CTX
HiRIC

ABSTRACT

High-resolution topographic mapping is essential for scientific investigations and operational exploration of planets, such as Mars. Photoclinometry, which uses light scattered from a surface to reconstruct 3D topography, can retrieve subtle topographic details from monocular images. However, its performance is affected by the atmosphere of Mars, which alters surface reflectance mechanisms due to the scattering and absorption by aerosols. Therefore, specific treatments accounting for these atmospheric effects are needed to enable photoclinometric mapping of Mars. This paper presents a novel photoclinometric approach incorporating a radiative-transfer model of atmospheric scattering effects for pixel-wise 3D reconstruction of the Martian surface. The approach requires a high-resolution image, a corresponding coarse-resolution digital elevation model (DEM), and information of the optical depth as inputs. A radiative transfer model adapted to the Martian atmosphere is used to account for the atmospheric effects. The approach also allows directly adopting optical depth estimates from a global database (e.g., the Mars Climate Database). The approach was validated using different types of Mars orbiter images collected by cameras on-board the Mars Reconnaissance Orbiter and the Tianwen-1 Orbiter. The results indicate that the approach can achieve a geometric accuracy (in terms of root-mean-squared error (RMSE) of the elevation) of approximately 2 pixels of the image resolution and significantly enhances topographic details. In addition, we evaluated the approach using different settings for the optical depths and spatial resolutions of the input DEMs. The results show that overestimating the optical depth leads to overestimation of topographic amplitudes (e.g., deeper craters). On the other hand, underestimating the optical depth by the same amount as overestimation leads to a smaller increase in the RMSE. Moreover, coarsening the resolution of an input DEM increases the RMSE of the photoclinometric results. Nevertheless, photoclinometry improves both the RMSE and the resolution of the input DEM. This new approach serves as an effective means for applying photoclinometry for pixel-wise 3D topographic mapping of the Martian surface. This will facilitate exploitation of the large number of high-resolution monocular images of Mars in 3D topographic mapping of the planet.

1. Introduction

High-resolution topographic maps (such as digital elevation models, DEMs) of the Martian surface are essential for many aspects of Mars exploration. For instance, DEMs of the Martian surface have supported a spectrum of scientific investigations, such as the characterisation of surface landforms (Goudge et al., 2017), atmospheric dust (Petrova et al., 2012), and the deduction of the geologic history of regions of interest (Schon et al., 2012; Bell et al., 2022). DEMs also play a vital role in landing-site mapping and selection (Kirk et al., 2008; Wu et al., 2021a, 2021b, 2022; Lorenz, 2023), and navigation and path planning for surface-operating rovers (Carsten et al., 2007), to ensure successful Mars exploration and maximise the scientific value of such missions.

Remote sensing observations are the predominant data sources for deriving the topography of the red planet. Image data collected by orbiter cameras, such as the High-Resolution Stereo Camera (HRSC) (Neukum et al., 2009) on-board the Mars Express, the Context Camera (CTX) (Bell et al., 2013) and the High-Resolution Imaging Science Experiment (HiRISE) (McEwen et al., 2007) on-board the Mars Reconnaissance Orbiter, are important remote-sensing observations. With the

* Corresponding author at: Planetary Remote Sensing Laboratory, Department of Land Surveying and Geo-Informatics | Research Centre for Deep Space Explorations, The Hong Kong Polytechnic University, Hung Hom, Kowloon, Hong Kong, China.
E-mail address: bo.wu@polyu.edu.hk (B. Wu).

https://doi.org/10.1016/j.isprsjprs.2023.09.017
Received 13 May 2023; Received in revised form 19 September 2023; Accepted 19 September 2023
Available online 25 September 2023

success of China's Tianwen-1 Mars mission, the High-Resolution Imaging Camera (HiRIC) (Meng et al., 2021) and Moderate Resolution Imaging Camera (Tan et al., 2021) on board the Tianwen-1 orbiter have emerged as new data sources for mapping Mars. Traditionally, images are processed by stereo photogrammetry to extract three-dimensional (3D) information of a surface from multi-perspective overlapping images (Shan et al., 2005; Gwinner et al., 2009; Li et al., 2022). However, photogrammetry requires stereo coverage of a given region. Photoclinometry (Rindfleisch, 1966; Kirk, 1987) is an alternative method that derives 3D topographic information from image brightness and can be implemented using a single image. The technique has been applied to landing site mapping in previous planetary missions (Beyer et al., 2003; Beyer & Kirk, 2012; Beyer, 2017; Wu et al., 2021a). Photoclinometry is more effective than photogrammetry in retrieving subtle surface details (e.g., of a boulder that is a few pixels wide), while photogrammetry is better at retaining the overall geometric accuracy (Kirk, 1987; Wu et al., 2018). In this context, photoclinometry and photogrammetry are complementary and have been integrated to realise effective 3D mapping of the lunar surface. However, to apply photoclinometry to Mars, it is necessary to address the effects of the atmosphere on the brightness of image pixels. Previous works have devised different solutions to account for such effects (e.g., Gehrke, 2008; Jiang et al., 2017; Hess et al., 2022). On the other hand, the Martian sky exhibits significant forward scattering characteristics, so the brightness of the sky is not uniform (Thomas, 2001). This non-uniformity has not been thoroughly considered in previous solutions, which is therefore worth understanding its effects on the application of photoclinometry on Mars.

Therefore, in this study, we developed a novel photoclinometric approach for pixel-wise 3D reconstruction of the Martian surface considering the photometric effects of the Martian atmosphere. This approach requires a high-resolution image, a corresponding coarse-resolution DEM, and information of the optical depth (when the image is captured) as inputs. A radiative transfer model is used to account for the anisotropic scattering effects of the atmosphere. The approach was validated using three types of orbital images of Mars, i.e., those captured by HiRISE, HiRIC and CTX. In addition, we evaluated the effects of the optical depth, a key parameter for characterising the photometric effects of the atmosphere, and the spatial resolution of the input DEM on the reconstruction performance of the approach.

The remainder of the paper is organised as follows. Section 2 provides a brief review of the related works. Section 3 describes the atmosphere-aware photoclinometry approach for the 3D reconstruction of the Martian surface. Section 4 describes the validation of the approach using images from different Mars orbiters. Section 5 provides extended analyses and comparisons. Section 6 presents the concluding remarks.

2. Related work

2.1. Photoclinometry for planetary 3D mapping

Photoclinometry relies on the photometric relationship between the topography of the surface and the radiance that it reflects or scatters and is detected by a sensor to reconstruct surface topography from an image. Photoclinometry is also known as shape-from-shading and is a photometric method that was applied to planetary 3D mapping more than half a century ago (van Diggelen, 1951; Rindfleisch, 1966). This approach estimates topographic slopes from images by using a bidirectional reflectance distribution function (BRDF) model (Nicodemus et al., 1977), which correlates the surface slopes with pixel intensities, and then integrates the pixel-wise slopes to a surface model (e.g., a DEM). In this manner, photoclinometry can produce pixel-wise high-resolution DEMs of the surface from a single image. Photoclinometry is complementary to classical 3D mapping techniques, such as photogrammetry (Gwinner et al., 2009; Henriksen et al., 2017) and laser altimetry (Smith et al., 2001, 2010; Barker et al., 2021). The integration is usually realised by applying the technique to the DEMs produced by the later methods (Kirk et al., 2003a, Kirk et al., 2003b, 2022; Grumpe et al., 2014; Alexandrov & Beyer, 2018; Wu et al., 2018). Other types of integration use photoclinometry to handle specific challenges in classical methods, such as image matching in photogrammetry (Heipke, 1992; Liu & Wu, 2020). The integration with photoclinometry improves the limitations in conventional planetary 3D mapping, such as limited photogrammetric stereo coverage and sparse laser measurements due to orbital constraints. Notably, photoclinometry is often mentioned in works dedicated to the emerging deep-learning-based 3D mapping methods (Chen et al., 2021; Chen et al., 2022; Tao et al., 2021) since they share similar capabilities, such as being applicable to a single image. A method of applying photoclinometry to deep-learning derived DEMs is also found as an attempt to enhance the recovery of topographic details (Chen et al., 2022).

Photoclinometry can be applied to a single image (Grumpe et al., 2014; Kirk et al., 2003a,b; Liu and Wu, 2020; Wu et al., 2018, 2020) or multiple overlapping images (i.e., photometric stereo) (Woodham, 1980; Lohse et al., 2006; Alexandrov & Beyer, 2018; Liu et al., 2018). Early applications of planetary photoclinometry (van Diggelen, 1951; Horn, 1977) focused on single-image cases due to limited observations, which generated one-dimensional topographic profiles parallel to the solar direction; these are known as characteristic strips because the topographic slopes along such directions significantly affect the observed image radiance (Horn, 1977, 1990). A photoclinometric DEM can be produced by combining adjacent characteristic strips. However, this combination results in inconsistencies between adjacent strips due to albedo variations and the lack of connections between strips (Kirk, 1987; Kirk et al., 2003a, Kirk et al., 2003b). Single-image photoclinometry was later developed to directly generate DEMs (Wildey, 1975; Kirk, 1987; Horn, 1990) by considering geometric constraints, such as smoothness and integrability terms (Kirk, 1987; Frankot & Chellappa, 1988; Horn, 1990).

Photoclinometry is sensitive to variations in surface albedo (Kirk et al., 2003a, Kirk et al., 2003b; Bertsatos & Makris, 2010; Grumpe et al., 2014; Liu & Wu, 2021), less effective in reconstructing low-frequency topographic trends (Grumpe et al., 2014; Wu et al., 2018), and requires additional information to preserve the absolute elevation reference. In the single-image case, variations in surface albedo have been addressed by using images with desirable illumination conditions (Liu & Wu, 2021) and imposing statistical constraints (Lee & Rosenfeld, 1983; Huang & Mumford, 1999; Barron & Malik, 2011). Moreover, the performance can be improved by incorporating existing coarse-resolution DEMs (Grumpe et al., 2014; Jiang et al., 2017; Alexandrov & Beyer, 2018; Korokhin et al., 2018; Wu et al., 2018; Liu & Wu, 2020), such as those derived from photogrammetry and/or laser altimetry. Specifically, coarse-resolution DEMs provide plausible initial estimates of surface topography and its corresponding surface albedo and constrain topographic trends as well as an absolute elevation reference to the photoclinometric reconstruction. Thus, their introduction can facilitate the reconstruction of fine-scale surface details with high accuracy. Methods integrating photoclinometry and photogrammetry and/or laser altimetry have been successfully applied to the 3D mapping of celestial bodies, such as those of the Moon (Grumpe et al., 2014; Jiang et al., 2017; Korokhin et al., 2018; Wu et al., 2018; Liu & Wu, 2020), Mars (Jiang et al., 2017; Li et al., 2021; Hess et al., 2022), Mercury (Tenthoff et al., 2020), and several asteroids (Gaskell et al., 2008). There are also planetary photoclinometry software publicly available, such as the *pcsi/pc2d* tool in the Integrated Software for Imagers and Spectrometers 2 (ISIS2) of the United States Geological Survey (USGS) (Kirk et al., 2003a, Kirk et al., 2003b) and the *sfs* tool in NASA's Ames Stereo Pipeline (ASP) (Alexandrov & Beyer, 2018). Both tools offer the option to incorporate *a priori* DEM and deal with albedo variations to a certain extent. Particularly, ASP's *sfs* tool can be applied to multiple overlapping images. However, the *sfs* tool is currently not available for Mars mapping because of the atmospheric effects (Alexandrov & Beyer, 2018). An

extensive comparison between the two software tools can be found in Kirk et al. (2022).

2.2. Influences of atmospheric scattering on photoclinometry

When applying photoclinometry to Mars or other celestial bodies with atmospheres, it is necessary to account for the atmospheric scattering process, as this affects photometric interpretations of surface geometries (e.g., Davis & Soderblom, 1984; Jankowski & Squyres, 1991; Kirk et al., 2001; Kirk et al., 2003a, Kirk et al., 2003b; Hess et al., 2022). For Mars, there are several practical ways to minimise such effects. They include subtracting from the image the pixel values of shadows (Davis & Soderblom, 1984; Jankowski & Squyres, 1991), using a linear approximation model for atmospheric correction (Kirk et al., 2003a, Kirk et al., 2003b; Gehrke, 2008), and iteratively search for the appropriate atmospheric correction parameters until photoclinometry best fits an *a priori* DEM (Kirk et al., 2003a, Kirk et al., 2003b). To this end, the surface BRDF model and photometric processes of atmospheric dust and gas can be incorporated into a top-of-the-atmosphere (TOA) photometric model to mimic the radiance observed by a sensor above a celestial body's atmosphere. TOA photometric models are essential for a range of applications in Mar science, such as cartography and mapping (Kirk et al., 2001; Gehrke, 2008; Hess et al., 2022), and atmospheric studies (Hoekzema et al., 2011; Petrova et al., 2012; Liu et al., 2022). A TOA model may be simple or complex, depending on the use case, but all such models require optical depth as a parameter, as it is related to the turbidity of an atmosphere. Optical depth can be retrieved using cameras onboard landers and rovers such as Viking landers, Mars Exploration Rovers (MERs) and Mars Science Laboratory (MSL) (Lemmon et al., 2015; Chen-Chen et al., 2019) or sensors onboard satellites such as Mars Color Imager (MARCI), CRISM and OMEGA (Ceamanos et al., 2013; Vincendon, 2007).

Sophisticated TOA models (Petrova et al., 2012; Fernando et al., 2015, 2016; Liu et al., 2022) require the scattering properties of atmospheric dust (Tomasko et al., 1999; Wolff et al., 2009; Chen-Chen et al., 2019) and introduce radiative transfer models (RTMs) (e.g., Stamnes et al., 1988; Mishchenko & Travis, 1997) to simulate the radiance propagation of an atmosphere. TOA models of Mars typically assume that it has a uniform skylight (i.e., the sky is equally bright in all viewing directions) (Petrova et al., 2012; Hess et al., 2019, 2022; Liu et al., 2022). However, the Mars atmosphere exhibits apparent anisotropic skylight (Davis & Soderblom, 1984; Thomas, 2001; Spiga & Forget, 2008). Its implications for Mars photoclinometry have been explicitly discussed by Kirk et al. (2001). Yet applications of Mars photoclinometry with considerations to anisotropic skylight are not common and therefore worth further investigation.

3. An atmosphere-aware photoclinometric approach

3.1. Overview of the approach

The workflow of the approach is illustrated in Fig. 1. First, a high-resolution image and corresponding initial coarse-resolution DEM are provided as inputs, of which the latter can typically be obtained from existing DEM data generated from photogrammetry or laser altimetry. The image is ortho-rectified and co-registered with this DEM. Then, the image and DEM are forwarded to a DEM-constrained hierarchical photoclinometric 3D reconstruction module, which reconstructs the detailed topography observed in the image to a high-resolution DEM. The photoclinometric process involves the following steps. Based on the image and known illumination and imaging geometry, the surface albedo and reflectance per image pixel are iteratively refined, and the DEM is optimised according to the surface reflectance. A TOA photometric model, with specific considerations pertaining to the scattering anisotropy of the atmosphere, is used to account for the disturbance of surface reflectance due to the atmosphere of Mars to obtain the most

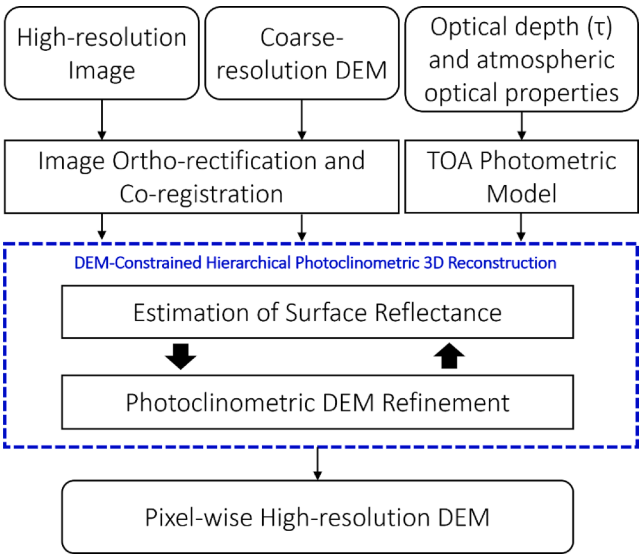

Fig. 1. Workflow of the atmosphere-aware photoclinometric approach.

plausible surface reflectance. The input coarse-resolution DEM provides the initial condition and constraints. The output is a photoclinometrically refined high-resolution DEM with topographic details up to the pixel level of the image.

3.2. TOA photometric model for Mars imaging observations

3.2.1. A TOA model considering atmospheric scattering and anisotropic skylight effects

The TOA photometric model describes the radiance observed by a sensor after it interacts with a planetary atmosphere and surface. In general, the radiance propagation process of bodies with atmospheres can be broken down into several components (Petrova et al., 2012), encompassing the direct and indirect reflectances at the surface and photometric interactions with the aerosols.

The TOA photometric model requires the optical depth and aerosol scattering properties of the Martian atmosphere, which can be obtained through image-based methods (Hoekzema et al., 2011; Liu et al., 2022), from the Mars Climate Database (MCD) (Montabone et al., 2015), and from other studies that have been dedicated to the scattering parameterisation of Martian dust (Ockert-Bell et al., 1997; Tomasko et al., 1999; Wolff et al., 2009; Chen-Chen et al., 2019). An RTM is then built to model the angular distribution of the solar radiation reaching the surface and the radiation that reaches the sensor without interacting with the surface. These two quantities are used to construct the TOA photometric model for the imaging scene.

For practical reasons, the TOA models used for Mars remote sensing are often simplified (i.e., only the important components of the full model are implemented) (Gehrke, 2008). Based on the formulations by Hess et al. (2019, 2020), which represent the more rigorous versions among the available strategies, we further develop the TOA model by incorporating the scattering characteristics of Martian aerosols and resultant anisotropic skylight (Davis & Soderblom, 1984; Thomas et al., 1999; Kirk et al., 2001). Our TOA model is formulated as follows:

$$I_{TOA} = \omega e^{-\tau\left(\frac{1}{\mu_{0F}}+\frac{1}{\mu_F}\right)} R_{dd}(\mu_0,\mu) + \omega e^{-\tau\frac{1}{\mu_F}} R_{hd}(\mu_0,\mu,\tau) + \alpha(\tau) \quad (1)$$

where I_{TOA} is the TOA radiance factor observed by the sensor, ω is the surface albedo, and τ is the atmospheric optical depth. μ_{0F} and μ_F are the incident and emission angle cosines relative to the local geodesic flat surface, respectively. R_{dd} is the bidirectional surface reflectance, and R_{hd} is the atmospherically-illuminated-directional reflectance (i.e., the

reflectance of the surface illuminated by the scattered light of the atmosphere), which is similar to hemispherical-directional reflectance but considered anisotropic skylight instead of a diffuse uniform skylight. Because the anisotropy of the Martian skylight is considered, R_{hd} depends on the surface orientation (i.e., μ_0 and μ) unlike that used by Hess et al. (2019, 2020). $e^{-\tau\frac{1}{\mu_{0F}}}$ and $e^{-\tau\frac{1}{\mu_F}}$ are the atmospheric attenuation factors of the incident and reflected light, respectively, modelled based on the Beer-Lambert law. Because R_{dd} is affected by the atmospheric attenuation of both incoming and outgoing light, its attenuation factor is $e^{-\tau\frac{1}{\mu_{0F}}} \times e^{-\tau\frac{1}{\mu_F}} = e^{-\tau\left(\frac{1}{\mu_{0F}}+\frac{1}{\mu_F}\right)}$. In contrast, R_{hd} is affected only by the attenuation of the outgoing light because the scattering and attenuation of the incoming light are considered by R_{hd}. $\alpha(\tau)$ corresponds to aerosol path scattering that never interacts with the surface. The contribution of R_{hd} becomes more significant as τ increases, implying an increase in the turbidity of the atmosphere (Spiga & Forget, 2008). If τ is too large, the contributions of both R_{dd} and R_{hd} decrease because the atmosphere is too thick and tends to block most of the incoming sunlight, with α increasing monotonically with τ. R_{hd} and $\alpha(\tau)$ can be modelled using RTMs (Petrova et al., 2012) or Monte Carlo simulations (Vincendon et al., 2007). In either case, the photometric properties of the atmosphere must be known. It is important to note that Eq. (1) still neglects some scattering processes. The first component that becomes evident is the scattered beam resulting from R_{dd} and R_{hd} being further scattered by the atmosphere before reaching the sensor. This indirect scattering of the reflected beam is neglected due to computation complexities. The second ignored component is the light that is scattered by the surface to the atmosphere and then scattered back to the surface (i.e., surface-sky-surface scattering). This component is ignored to avoid prior knowledge of surface albedo. A brief estimate of the effects of neglecting the second component is given in Section 3.2.2.

3.2.2. Photometric modelling of the Martian surface

The TOA model described by Eq. (1) exhibits two types of photometric processes related to the Martian surface: R_{dd} and R_{hd}. R_{dd} is used to model the surface reflectance that is illuminated by direct sunlight and then propagated directly to the sensor, whereas R_{hd} models the surface reflectance that is illuminated from multiple directions by the atmosphere and then propagated directly to the sensor. R_{dd} and R_{hd} are theoretically related because they are governed by the scattering mechanisms of the same surface.

R_{dd} can be described using various photometric models (Fairbairn, 2005; Soderblom et al., 2006; Shkuratov et al., 2011; Hapke, 2012). In Eq. (1), R_{dd} and R_{hd} are linearly dependent on the surface albedo ω; therefore, we select a photometric model with similar properties, i.e., the lunar Lambert model (LL model) (McEwen, 1991, 1996) to model the bidirectional reflectance, which has also been applied to Mars studies (Soderblom et al., 2006). Other photometric models that are linearly dependent on ω can also be used (e.g., Minnaert, 1941; Fairbairn, 2005). However, for photometric models that are non-linearly dependent on ω, such as the Hapke model (Hapke, 2012), Eq. (1) should be modified to account for the non-linearity. The LL model, which is a linear combination of the Lambert model and Lommel-Seeliger model, is formulated as

$$R_{dd}(\mu_0,\mu,g) = \left[(1-\lambda(g))\mu_0 + 2\lambda(g)\frac{\mu_0}{\mu_0+\mu}\right]p(g) \tag{2}$$

where μ_0 and μ are the incident and emission angle cosines relative to the surface normal, respectively. $\lambda(g)$ depends on the phase angle g and controls the relative contribution of the two major components within the model. $\lambda(g)$ and $p(g)$ dedicated to Mars are derived using the parameters from the documentation of the Photomet application in USGS's ISIS: (https://isis.astrogeology.usgs.gov/Application/presentation/Tabbed/photomet/photomet.html, example 7). The adopted parameters are a list of values corresponding to a definite set of g, hence interpolation is necessary to compute the desired function outputs for R_{dd}.

R_{hd} describes the light reflectance of a surface that is illuminated by the atmosphere. As illustrated in Fig. 2, we consider a hemispherical sky-dome in which sunlight propagates downwards (Fig. 2a). The local terrain (Fig. 2b) forms an angle with the sky-dome based on its surface orientation, and therefore only part of the sky-dome irradiance reaches the surface (Fig. 2c), and the rest is occluded (Fig. 2d). Illumination from below the horizon reaching the surface (Fig. 2e) is assumed to be negligible. We model R_{hd} by integrating R_{dd} over all possible illumination directions in the upper hemisphere of the surface for the same outgoing direction, as follows:

$$R_{hd}(\mu_0,\mu,\tau) = \int_{\phi=0}^{2\pi}\int_{\theta=0}^{\pi/2}\beta(\phi,\theta,\tau)R_{dd}(\mu_0,\mu,g) \tag{3}$$

where ϕ is the illumination azimuth and θ is the illumination zenith in radians. $\beta(\phi, \theta, \tau)$ denotes the illumination propagated by the atmosphere to the direction defined by ϕ and θ, which can be modelled using RTMs similar to $\alpha(\tau)$ in Eq. (1). The integration over the sky-dome covers all of the illumination azimuths ($0 \le \phi \le 2\pi$) and zeniths ($0 \le \theta \le \pi/2$). $\beta(\phi, \theta, \tau)$ below the horizon (Fig. 2e) is considered to be negligible and is thus not included. μ_0 depends on the surface orientation and skylight illumination vector defined by ϕ and θ. Illumination directions beyond the visible range of the surface yield an invalid μ_0, and so the corresponding R_{dd} is nullified. Therefore, Eq. (3) naturally accounts for the sky-view factor. Because the illumination direction varies, the phase angle g changes with ϕ and θ. To account for the complexity of $\beta(\phi, \theta, \tau)$ and R_{dd}, R_{hd} is computed based on numerical integration of a set of predefined μ_0 and μ, with ($0 \le \mu_0, \mu \le 1$) and a known τ. R_{hd} for any specific μ_0 and μ is then interpolated from the set.

3.2.3. Photometric modelling of the Martian atmosphere

Photometric modelling of the Martian atmosphere requires two components: (1) single scattering characteristics of the aerosols, which governs how light is absorbed and scattered by the Martian atmospheric dust; and (2) an RTM that reproduces how light is propagated through the atmosphere, given the aerosol scattering properties.

The scattering properties useful for the photometric modelling of Martian aerosols include the single scattering albedo of the aerosols ω_{atm}, phase function $p_{atm}(g)$, and parameters used to characterise $p_{atm}(g)$. ω_{atm} determines the amount of light absorbed by the aerosols and propagated onwards. $p_{atm}(g)$ describes how aerosol particles or clusters scatter incoming light at different phase angles. The parameters required by $p_{atm}(g)$ depend on the chosen model. We select the single Henyey-Greenstein phase function (Pollack et al., 1995) over the alternative models (Chen-Chen et al., 2019; Mishchenko, 2020) owing to its simplicity and the availability of parameters dedicated to Mars. The single Henyey-Greenstein function is formulated as follows:

$$p_{atm}(g) = \frac{1-\varepsilon^2}{[1+\varepsilon^2+2\varepsilon cos(g)]^{3/2}} \tag{4}$$

where g is the phase angle, and $-1 \le \varepsilon \le 1$ is the asymmetry factor characterising the directional preference of the scattering particle. $\varepsilon > 0$ implies more forward scattering and $\varepsilon < 0$ suggests the opposite. The parameters ε and ω_{atm} vary with the wavelength and should therefore be chosen according to the radiometric properties of the target image. The centre wavelengths of the HiRISE, HiRIC and CTX images considered in this research are 700 nm (McEwen et al., 2007), 675 nm (Meng et al., 2021), and 611 nm (Bell et al., 2013), respectively. Thus, we use the scattering parameters of Martian aerosols at similar wavelengths reported by Ockert-Bell et al. (1997): $\omega_{atm} = 0.94$ and $\varepsilon = 0.65$, which have also been used by Spiga and Forget (2008) and Liu et al. (2022).

We apply the Discrete Ordinate Radiative Transfer (DISORT) program (Stamnes et al., 1988), which has been widely adopted in planetary photometry (McGuire et al., 2008; Doute & Ceamanos, 2010;

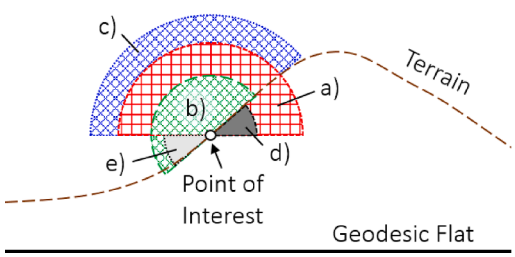

a) Sky-dome (red)
b) Terrain upper-hemisphere (green)
c) Sky-dome not occluded by the local terrain (blue)
d) Sky-dome occluded by local terrain (dark grey)
e) Terrain upper-hemisphere assumed to not be illuminated by the sky-dome (light grey)

Fig. 2. Conceptual illustration of sky-dome illumination.

Hapke, 2012; Ceamanos et al., 2013; Jiang et al., 2017; Chen-Chen et al., 2019), to calculate $\alpha(\tau)$ in Eq. (1) and $\beta(\phi, \theta, \tau)$ in Eq. (3). We consider a single layer of the atmosphere characterised by the abovementioned photometric properties of the aerosols and a known τ. A perfectly absorbing surface (i.e., $\omega = 0$) is assumed to be present at the lower boundary of the atmosphere. For simplicity, we do not consider more complex aspects, such as multiple atmospheric layers, air temperature, and pressure. Such a simplified configuration is considered valid for $\tau \leq 1$ (Vincendon et al., 2007; Petrova et al., 2012; Liu et al., 2022). In addition, we assume that $\beta(\phi, \theta, \tau)$ is independent of surface scattering, i.e., the surface-sky-surface scattering is ignored, an assumption also used by several other works (e.g., Hess et al., 2022; Liu et al., 2022). Consequently, prior knowledge of the surface is not required to construct the atmospheric model. Subsequently, we configure the directions of the incident and emerging beams according to the illumination and imaging geometry of the image to be analysed. Based on the constructed RTM, we extract the quantities $\alpha(\tau)$ and $\beta(\phi, \theta, \tau)$. $\alpha(\tau)$ is characterised by the intensity of the emerging beam leaving the TOA (i.e., the upper boundary of the atmosphere) and travelling towards the sensor. For $\beta(\phi, \theta, \tau)$, we first discretise the downward propagating hemisphere into multiple streams (i.e., $\phi_{k\in K}$, $\theta_{k\in K}$, where K is the number of streams) and use DISORT to compute the flux of each stream reaching the bottom layer. The resulting set of $\beta(\phi, \theta, \tau)$ produces a panorama of the sky-dome (Fig. 3), which is then used to compute R_{hd}. Here we briefly analyse the impacts of ignoring the surface-sky-surface scattering, β_{sks}. We first approximate β_{sks} as the product of the bi-hemispheric reflectance (Bond Albedo) of the Martian surface $Bond_{surf}$, which is 0.25 for Mars, and that of the Martian atmosphere, $Bond_{atm}(\tau)$. That is $\beta_{sks}(\tau) = Bond_{surf} \times Bond_{atm}(\tau) = 0.25 Bond_{atm}(\tau)$. For reference, using the selected aerosol scattering parameters, $\omega_{atm} = 0.94$ and $\varepsilon = 0.65$, we get $Bond_{atm}(1.0) = 0.2$ and $Bond_{atm}(2.0) = 0.284$. We also compute the total amount of incident light on a surface, which is the sum of direct sunlight and total β (i.e., the angular integral of Fig. 3) and β_{sks}. The ratio of β_{sks} relative to the total incident light then gives an estimate of how much light is ignored when neglecting β_{sks}. We simulated several practical scenarios: incidence angle = {40°, 50°, 60°} and emission angle = 0°. We then found that at a 40° incidence angle, 10 % of total incident light is ignored for neglecting β_{sks} when $\tau = 1.43$. The 10 % limit becomes $\tau = 1.15$ for the 50° case and 0.87 for the 60° case, respectively. This is because at a larger incidence angle, incoming light travels a longer path which leads to a reduction in total light reaching the surface. As a result, the relative effects of neglecting β_{sks} increase. This analysis gives a brief estimate of the effects of ignoring β_{sks}, which can be within 10 % when the optical depth is lower than the aforementioned limits of the respective cases.

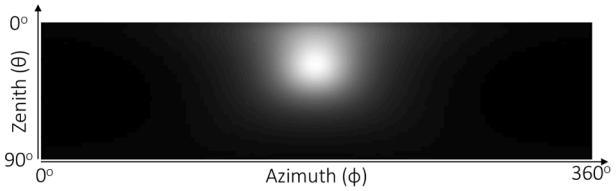

Fig. 3. Panorama of the Martian sky simulated by DISORT (The angle of incidence is set as 56.19° and τ is 0.43).

As exemplified in Fig. 3, the skylight produced by the Martian atmosphere (i.e., the set of $\beta(\phi, \theta, \tau)$) is anisotropic: Incoming skylight concentrates around the solar aureole and diminishes outwards. Therefore, Sun-facing surfaces naturally receive more skylight than surfaces facing away from the Sun. As τ increases, more multiple scattering and absorption occur within the atmosphere, resulting in more dispersed skylight illumination. The TOA model used in this study provides a more comprehensive treatment of the Martian skylight anisotropy, which has been typically simplified in other TOA models (Gehrke, 2008; Hess et al., 2019, 2020; Liu et al., 2022).

3.3. Photoclinometric 3D reconstruction of the DEM

The photoclinometric reconstruction module performs two key tasks: (i) refinement of the surface reflectance, and (ii) photoclinometric refinement of the DEM. The module iterates both steps consecutively until the topographic details are effectively imprinted onto the resulting DEM. First, we factorise Eq. (1) as follows:

$$I_{TOA} = \omega \left[e^{-\tau\left(\frac{1}{\mu_{0F}}+\frac{1}{\mu_F}\right)} R_{dd}(\mu_0, \mu) + e^{-\tau\frac{1}{\mu_F}} R_{hd}(\mu_0, \mu, \tau) \right] + \alpha(\tau)$$

$$I_{TOA} - \alpha(\tau) = \omega R_{surf}(\mu_0, \mu, \tau) \quad (5)$$

This form enables the direct computation of the unknown surface albedo because the combined surface reflectance (i.e., R_{surf}, defined in the square brackets) and $\alpha(\tau)$ can be obtained from the inputs. The optical depth τ can be obtained from the MCD (Montabone et al., 2015) or image-based methods (Hoekzema et al., 2011; Liu et al., 2022). There are also other practical methods to estimate τ such as dark pixel correction (Kirk et al., 2001) and iterative photoclinometry-based analysis (Kirk et al., 2003a, Kirk et al., 2003b; 2008). Then, based on Eq. (5), we initialise ω and R_{surf} for each pixel using the input DEM and image. At each iteration, pixel-wise albedo ω is refined by a local smoothing process, a strategy that has proven effective in previous works (Grumpe et al., 2014; Wu et al., 2018; Liu & Wu, 2020). Then, pixel-wise R_{surf} is gradually refined by enforcing Eq. (5). The DEM is then photoclinometrically adjusted by minimising the following term:

$$E_{img} = \left(R_{refined} - R_{DEM}\right)^2 \quad (6)$$

where $R_{refined}$ is the refined R_{surf}, and R_{DEM} is the corresponding value calculated from the DEM.

The input DEM provides the initial conditions and constrains the DEM refinement throughout the process. To this end, a coarse-resolution constraint is introduced, as follows:

$$E_{DEM} = \left[g(Z_{ini}, \sigma) - g(Z_{current}, \sigma)\right]^2 \quad (7)$$

where Z_{ini} is the input DEM, and $Z_{current}$ is the DEM being photoclinometrically optimised. $g(*, \sigma)$ is a Gaussian smoothing operator with σ as its predefined standard deviation. This constraint ensures that the resulting DEM is close to the input DEM at a coarse scale (Grumpe et al.,

2014; Jiang et al., 2017; Wu et al., 2018). Therefore, the complete error term becomes

$$E_{Total} = E_{img} + w_{DEM} E_{DEM} \tag{8}$$

where w_{DEM} is the weight for E_{DEM}. This weight is determined such that the DEM adjustments resulting from E_{DEM} do not neutralise those resulting from E_{img}; i.e., when E_{img} considerably affects the DEM, w_{DEM} is set high to ensure overall control, whereas when E_{img} modifies only subtle surface details, w_{DEM} is set low to provide sufficient freedom. This setting is incorporated automatically at the start of each iteration by statistically evaluating DEM adjustments of the previous iteration, thereby achieving self-adaption.

We introduce a relaxation strategy that discretises the complex global refinement task into pixel-wise local refinement tasks. Local optimisation of Eq. (8) is performed using the Levenberg-Marquardt algorithm. In addition, we apply a hierarchical refinement pipeline that initiates photoclinometry at a coarse spatial resolution and then gradually enhances the resolution until it reaches the pixel-scale of the image.

4. Experimental analysis

The proposed approach was tested using various Mars imaging data, namely HiRISE and CTX from the MRO and HiRIC from the Tianwen-1 orbiter. This section provides a demonstration of the method in applying to the aforementioned imaging data. In addition, the experimental datasets also laid a foundation for the extended analysis in section 5, which addresses several key issues related to photoclinometry.

4.1. HiRISE image of the Victoria crater

We first tested the photoclinometric approach using HiRISE data. The test site was the Victoria Crater, which has been extensively studied and was visited by the Opportunity rover. The inputs are a HiRISE image (0.25 m/pixel) (ID: TRA_000873_1780_RED, http://viewer.mars.asu.edu/planetview/inst/hirise/TRA_000873_1780_RED#P=TRA_000873_1780_RED&T=2) and a photogrammetric DEM (1 m/pixel) (ID: DTEEC_001414_1780_001612_1780_U01, https://www.uahirise.org/dtm/dtm.php?ID=PSP_001612_1780) generated from stereo HiRISE images. The HiRISE DEM was down-sampled to 8 m/pixel to account for local high-frequency noise. We extracted a subset of the region (5177 × 6856 pixels on the HiRISE image) for which the HiRISE DEM is available. The original HiRISE DEM also served as a reference. However, it is important to note that the photogrammetric generation of this reference HiRISE DEM was very challenging (Kirk et al., 2008): the area is almost featureless and there are vertical outcrops that are also affected by shadows, unfavoured for stereo image matching. As a result, the reference HiRISE DEM has a high level of noises at fine-scale and cannot resolve detailed topography such as Aeolian bedforms. The optical depth of the image was obtained from the direct measurements by the Opportunity rover (Lemmon et al., 2015). The characteristics of the selected HiRISE image are summarised in Table 1.

The experimental results are shown in Fig. 4. First, we visually compared the photoclinometric DEM (Fig. 4b) and photogrammetric DEM that serves as a reference (Fig. 4c). Both DEMs exhibited high correspondence, which is highly desirable. Further inspection revealed significant improvements in surface details, such as the sand ripples at the bottom of the Victoria Crater. Close-up views in Fig. 4d indicate that the photoclinometric result has more plausible surface details and less high-frequency noise than that based on the photogrammetric DEM. We derived an elevation difference map (Fig. 4e) between the reference DEM and photoclinometric DEM. The inconsistencies between the two were limited, with large differences observed near the rim of Victoria Crater, which has abrupt elevation changes. The overall geometric accuracy was also confirmed by the root-mean-squared deviations (RMSD) and maximum absolute elevation differences, which were approximately 0.5 m (2 pixels in the image space) and 6.8 m, respectively (Table 2). In addition to the elevation assessments, we computed the Pearson correlation coefficient (PCC_{img}) to assess the similarity between the shaded relief image generated from the DEM based on the same Sun illumination angles and the HiRISE image. The metric highlights the improved similarity ($PCC_{img} = 0.785$) of the photoclinometirc DEM with the input image compared with that associated with the photogrammetric DEM ($PCC_{img} = 0.453$). Note that the improved PCC_{img} means photoclinometry is reconstructing a DEM that is more visually desirable than the input and should not be taken as the sole indicator of improved geometric accuracy. The actual geometric correctness of the topographic details recovered by photoclinometry has to be assessed by geometrically comparison with a reference DEM.

Results of the examination of the two topographic profiles depicted in Fig. 4a are shown in Fig. 5. Profile 1 was a cross-section of the Victoria Crater, which can provide an overview of the overall geometric consistency. The profiles of the photoclinometric DEM (blue line) and the reference DEM (green dotted line) were highly overlapping, which indicates that the photoclinometric result was effectively constrained over coarse scales. The inset of profile 1 showed the magnified view of the bottom of the crater, which is characterised by groups of sand ripples. This indicates that the photoclinometric DEM recovered visually plausible geometries of the sand ripples, whereas the photogrammetric DEM exhibited noisy cross-sections, possibly due to challenges in image matching during photogrammetric processing such as repetitive patterns or homogeneous local textures on images. These results demonstrate the effectiveness of the photoclinometric approach in recovering surface details. Profile 2 crossed a group of small sand ripples and two small craters (marked by black arrows) southeast of Victoria. On the reference HiRISE DEM, these subtle landforms were either not visible or overwhelmed by noise, likely because of the challenges in photogrammetric image matching. In contrast, they were reconstructed in the photoclinometric result while maintaining overall consistency with the input. To better understand the 3D reconstruction accuracy of the fine-scale topography (e.g., sand ripples) of this area in the absence of an ultra-high resolution reference DEM, we briefly analysed the Aeolian bedforms distributed over the region. We found that the average slope of the sand ripples is ~5°. For reference, the reported average slope of Transverse Aeolian Ridges (TARs) on Mars is ~15° (Zimbelman, 2010). Although it may be possible that the sand ripples inside the Victoria crater are different from the typical Mars TARs, one cannot rule out the possibility that these features were underestimated due to suboptimal optical depth or other factors affecting photoclinometry. This also highlights the importance of a detailed and reliable reference DEM when assessing the performance of photoclinometry.

Table 1
Information of the tested HiRISE image (ID: TRA_000873_1780_RED).

Acquisition time	2006-10-03T12:44:13.425				
Optical depth (from Opportunity rover measurements)	0.43	Resolution (m/pixel)	0.25	Sub-solar azimuth (°)	299.14
Angle of incidence (°)	56.19	Angle of emission (°)	3.84	Phase angle (°)	59.31

4.2. HiRIC image of the Zhurong landing site

For the second experimental dataset, we selected the region surrounding the Tianwen-1 (Zhurong rover) landing site (Wu et al., 2022). The inputs include the Tianwen-1 HiRIC image (0.7 m/pixel) (Fig. 6a) and a photogrammetric DEM (3.5 m/pixel) (Fig. 6b) generated from stereo HiRIC images (Li et al., 2022). As can be noticed in Fig. 6b, we identified on the photogrammetric HiRIC DEM a line of artefact running vertically across the region. This artefact, which is likely produced during photogrammetric processing of multiple overlapping image

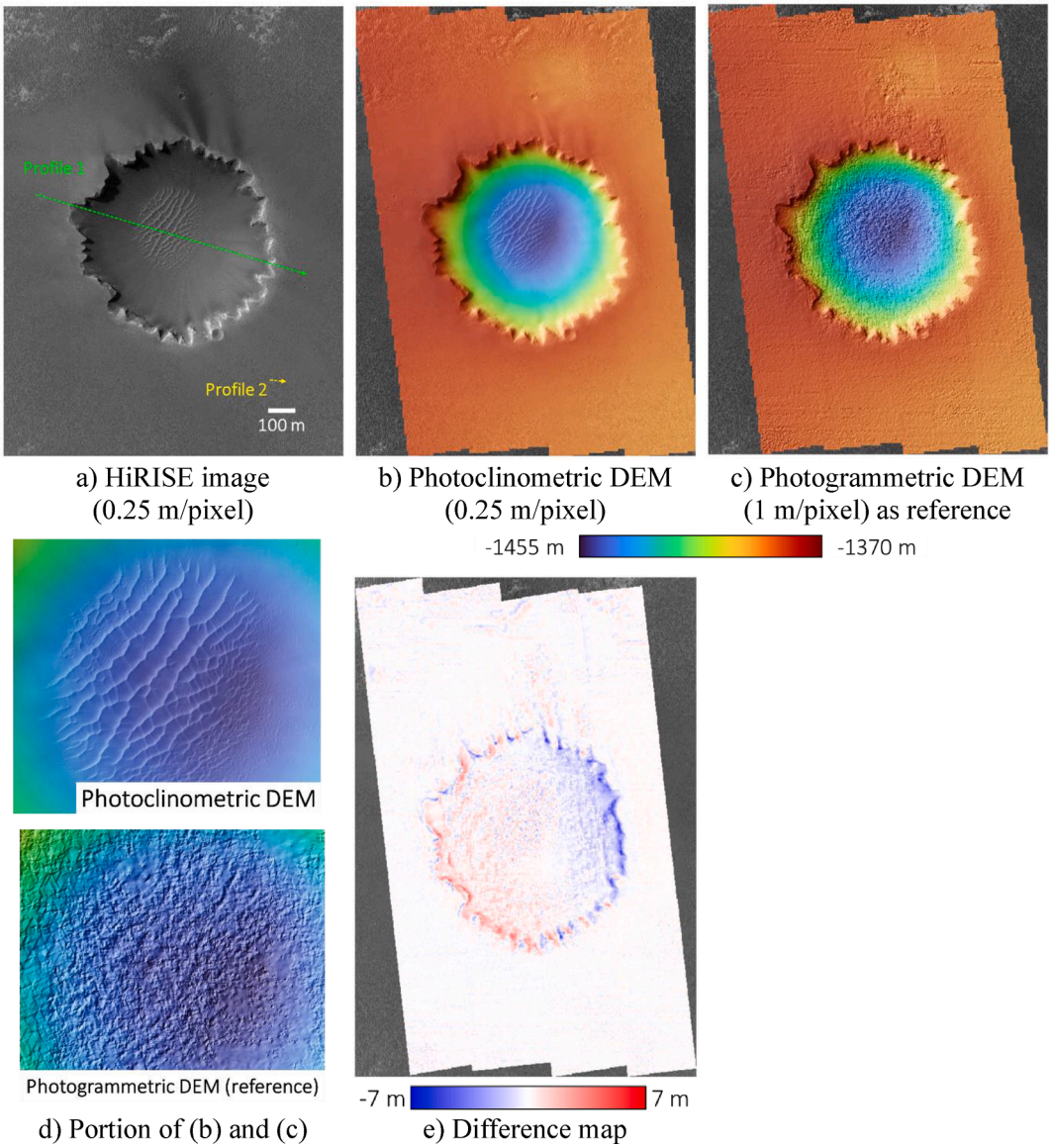

Fig. 4. Photoclinometric results for the Victoria Crater dataset.

Table 2
Overall quality metrics for the HiRISE dataset.

	Photoclinometric DEM (0.25 m/pixel)	Photogrammetric HiRISE DEM as reference (1 m/pixel)
RMSD (m)	0.5	N/A
Max. Abs. (m)	6.8	N/A
PCC_{img}	0.785	0.453

*PCC_{img} is the Pearson correlation coefficient of the computed shaded relief and input image.

strips, introduces height discontinuities of up to 2 m in the E-W direction. While the 2 m amplitude is not severe, the flat terrain of the region and the length of the artefact have made it distinctive. Therefore, to avoid photoclinometry inheriting this artefact and also to account for the lack of subtle surface details in this particular region, we downsampled the HiRIC DEM to 35 m/pixel as the input DEM. We extracted a subset of the region (2711 × 3809 pixels on the HiRIC image) near the Zhurong landing site. Moreover, we obtained the overlapping HiRISE DEM (Fig. 6d) to serve as a reference (ID: *DTEEC_069665_2055_069731_2055_A01*, 1 m/pixel). The optical depth of the image was inferred from an image-based approach presented by Liu et al. (2022). The characteristics of the selected HiRIC image are summarised in Table 3.

As shown in Fig. 6, the photoclinometric result (Fig. 6c) exhibited high visual correspondence with the reference photogrammetric DEM generated from the stereo HiRISE images (Fig. 6d). The magnified views of a local region (the box in Fig. 6d) in Fig. 6e show that the photoclinometric DEM revealed local scale landforms (e.g., small craters and Aeolian bedforms) and possessed less noise than the photogrammetric DEM from HiRISE images. The elevation difference maps (Fig. 6f and g) showed limited inconsistencies with the reference, larger elevation differences were observed on the photoclinometric DEM near the rim of the crater in the lower-left region, as in the case of the Victoria Crater. Closer inspection of this region revealed a group of small ripple-like bedforms, which were light-toned and accumulated near the crater rim. The presence of these bedforms, which exhibited increased surface roughness and albedo, may account for the higher overall brightness of this area. Table 4 shows that the overall RMSE of the photoclinometric DEM with respect to the reference DEM was about 0.8 m (less than 2 pixels in the HiRIC image space), similar to that of the photogrammetric HiRIC

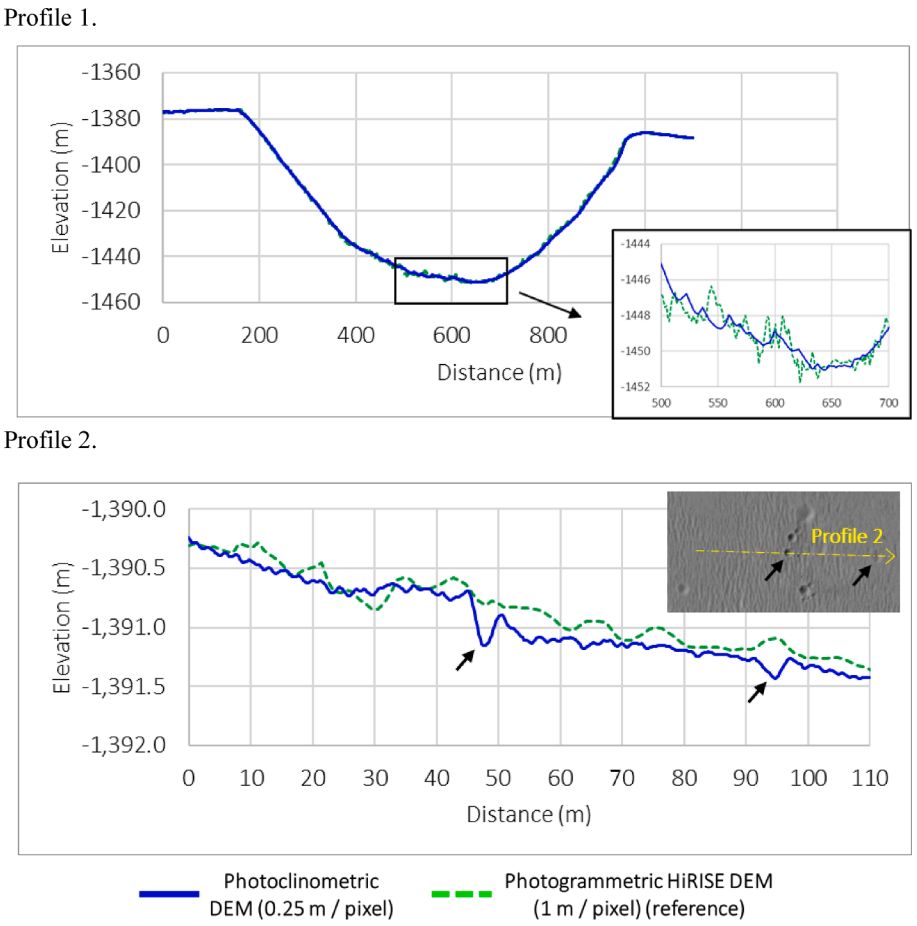

Fig. 5. Selected topographic profiles of the HiRISE dataset.

DEM. The maximum absolute error of the photoclinometric DEM was approximately 7.9 m, slightly higher than that of the photogrammetric HiRIC DEM (5.2 m) and attributable to the aforementioned crater rim areas. As indicated by the PCC_{img}, the photoclinometric result exhibited a much higher similarity with the input HiRIC image than other DEMs. Note that the HiRISE DEM's PCC_{img} and Fig. 6(e) have indicated that the DEM cannot provide a reliable reference for assessing the geometric correspondence of surface details up to the scale of the image. The situation can also be seen in the scale variations of RMS computed based on 0.7 m/pixel and plotted in Fig. 7. The two curves did not exhibit significant differences in the range of smaller k. A careful look would find that the reference DEM has partial topographic details (e.g., crests of Aeolian bedforms) mixed with greater uncertainties. The SNR is suboptimal which makes it less capable of assessing fine scale geometries. Nevertheless, the photogrammetric HiRIC DEM has the lowest RMS deviation of 0.733 m when the reference DEM is smoothed by a boxcar of width $k \approx 89$ pixels (~62 m), while the photoclinometric result has its lowest RMS deviation of 0.747 m at $k \approx 106$ pixels (~74 m).

Fig. 8 presents the profiles depicted in Fig. 6a. Profile 1 crossed two shallow craters west of the landing site. The two craters, that were not fully captured by the photogrammetric HiRIC DEM (red dashed line), were successfully reconstructed in the photoclinometric DEM (blue line), and their dimensions are consistent with those obtained using the photogrammetric HiRISE DEM (green dashed line). In addition, the overall geometry was similar to that obtained using the photogrammetric HiRISE DEM, owing to the high consistency between the input and the reference DEMs. Profile 2 shows the reconstruction result of a feature particularly challenging for photoclinometry. It presented the cross-section of a Traverse Aeolian Ridge (TAR) southwest of the landing site that is only partially resolved by the photogrammetric HiRIC DEM, but successfully reconstructed in the photoclinometric DEM. The TARs in this area are challenging for photoclinometry owing to the inherent characteristics of the technique (Jankowski & Squyres, 1991; Liu & Wu, 2021): they have a distinctively higher albedo than the surroundings, and the dominating topographic strike is along the north–south direction, nearly perpendicular to the illumination azimuth of the image (248°). The heights of the TAR measured from the profile of the photoclinometric DEM and photogrammetric HiRISE DEM were ~0.66 m (blue line) and ~0.72 m (green dashed line), respectively. The height of the TAR, based on measurements from the ground images by the Zhurong rover, was ~0.6 m (Liu et al., 2021), consistent with both measurements (with our result slightly closer). This finding shows that the photoclinometric approach recovered plausible dimensions of the TAR. Although the reconstruction of the right side of the TAR is not as desirable as its left side, its height is within a factor of 2 for this challenging feature.

4.3. CTX image of the Columbus Crater

The third experimental dataset focused on a region north-eastern of the Columbus Crater (Fig. 9). The inputs are a CTX image (5 m/pixel) (ID: J01_045278_1498_XN_30S165W, https://viewer.mars.asu.edu/viewer/ctx#P=J01_045278_1498_XN_30S165W&T=2) and the HRSC DEM (75 m/pixel) (http://viewer.mars.asu.edu/viewer/hrsc#T=0) covering the same region. We extracted a subset of the region (1576 × 3142 pixels on the CTX image) covered by a HiRISE DEM (1 m/pixel) (ID: DTEEC_010492_1510_045278_1510_A01, https://hirise.lpl.arizona.edu/PDS/DTM/PSP/ORB_010400_010499/PSP_010492_1510_ESP_045278_1510/DTEEC_010492_1510_045278_1510_A01.IMG) to serve as a reference. Because the reference HiRISE DEM has a much higher

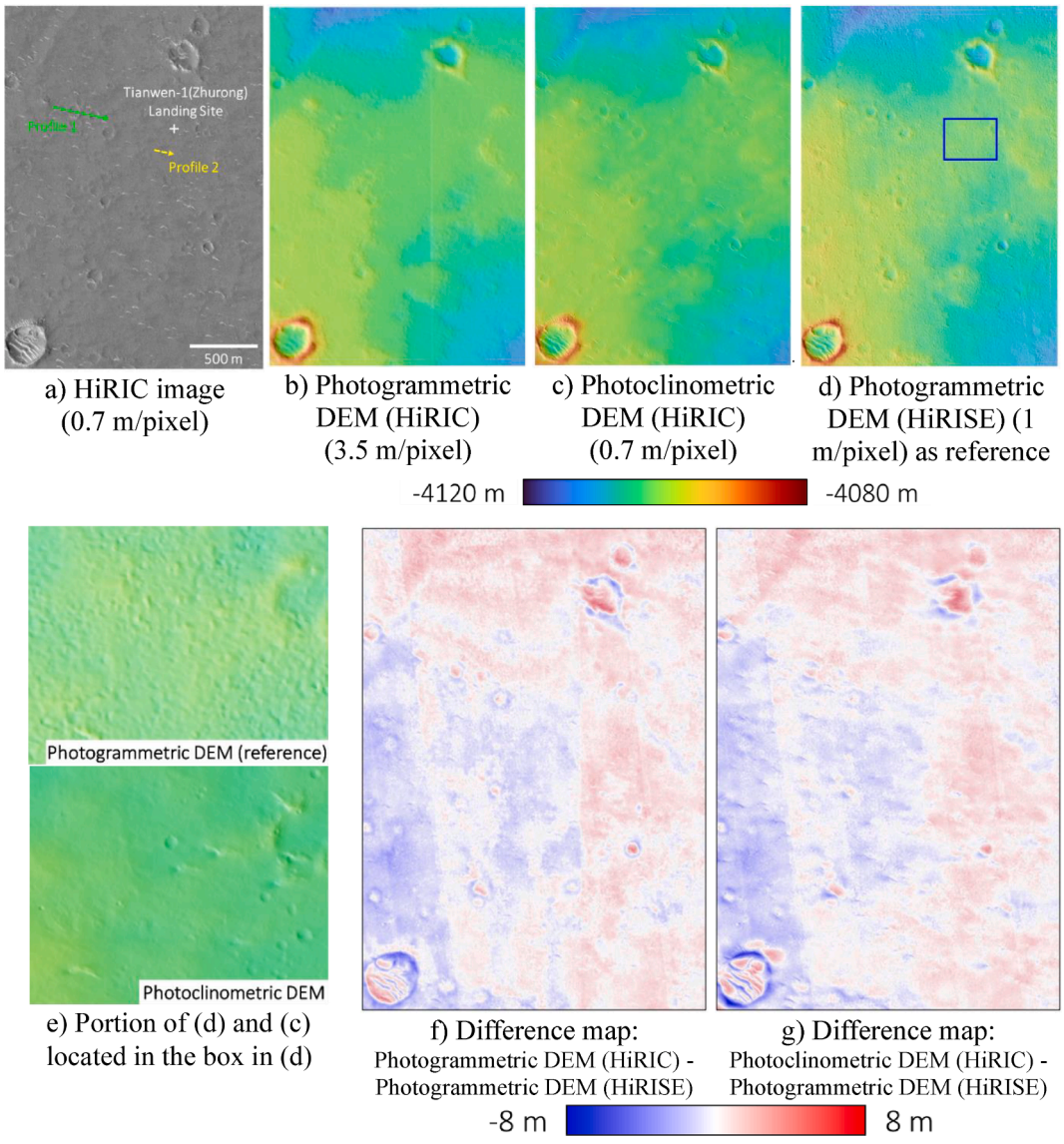

Fig. 6. Photoclinometric results for the HiRIC dataset.

Table 3
Information of the input HiRIC image (Orbit No. 0324).

Acquisition time	2021-03-24				
Optical depth (Liu et al., 2022)	0.5	Resolution (m/pixel)	0.7	Sub-solar azimuth (°)	248.0
Angle of incidence (°)	48.64	Angle of emission (°)	0.0	Phase angle (°)	48.64

Table 4
Overall quality metrics of the HiRIC dataset.

	Photogrammetric DEM (HiRIC) (3.5 m/pixel)	Photoclinometric DEM (HiRIC) (0.7 m/pixel)	Photogrammetric DEM (HiRISE) as reference (1 m/pixel)
RMSE (m)	0.80	0.83	N/A
Max. Abs. (m)	5.2	7.9	N/A
PCC_{img}	0.228	0.783	0.245

*PCC_{img} is the Pearson correlation coefficient of the computed shaded relief and input image.

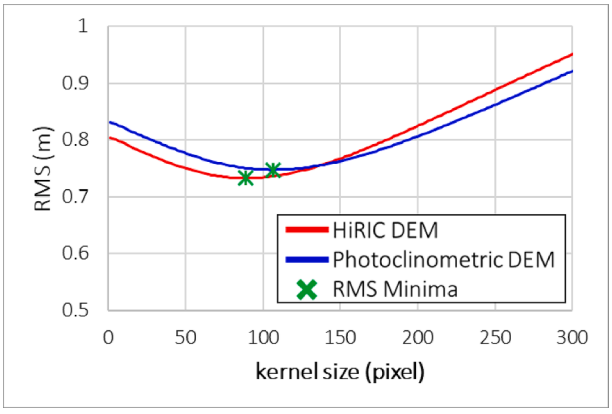

Fig. 7. DEM RMS at different scales for the HiRIC dataset.

spatial resolution than the input CTX image, we believe this experiment could help to clarify the absolute accuracy of the photoclinometric approach in Mars mapping applications. The optical depth of the image was obtained from the MCD (Montabone et al., 2015). The

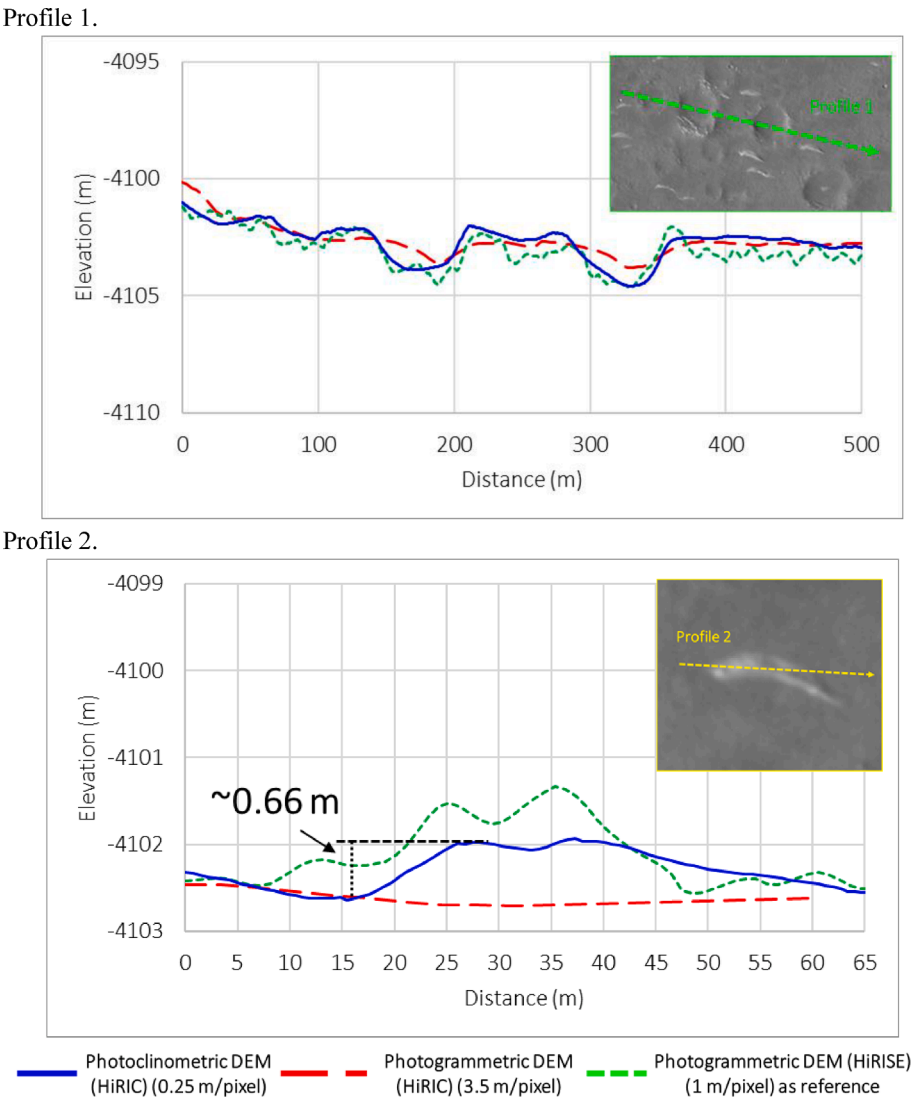

Fig. 8. Selected topographic profiles from the HiRIC dataset.

characteristics of the selected CTX image are summarised in Table 5.

The reconstruction results are presented in Fig. 9. Visual inspection revealed that the surface details presented on the CTX image (Fig. 9a) were successfully reproduced in the photoclinometrically reconstructed DEM (Fig. 9c), which exhibited strong correspondence with the HiRISE DEM (Fig. 9d). Fig. 9e shows the elevation difference map between the HRSC DEM used as the input and reference HiRISE DEM (i.e., error map), which exhibited considerable elevation differences along the transition zone between the highlands and lowlands and the patch of highlands located in the south. The photoclinometrically reconstructed DEM also exhibited similar spatial distributions (Fig. 9f), which implies that the result inherits the overall geometric quality of the input DEM. Fig. 9f also shows the strips associated with the down-Sun direction, which is known to be a challenge for single-image photoclinometry (Barron & Malik, 2011; Wu et al., 2018; Kirk et al., 2022). Moreover, the elevation differences of the photoclinometric result were lower than that of the input HRSC DEM, which indicates that the approach considerably enhances the geometric quality.

The overall absolute elevation differences are compared in Table 6. The RMSE decreased from 15.7 m for the HRSC DEM to 11 m (approximately 2 pixels in the image space) for the photoclinometirc CTX DEM, and the maximum absolute difference decreased from 63.8 m to 47 m for the corresponding entities. The metric PCC_{img} indicates there was a significant improvement in correspondence between the DEM and the input image after photoclinometry. In particular, the photoclinometric result outperforms the input HRSC DEM and the reference HiRISE DEM by a considerable margin in terms of the PCC_{img}. To assess the shape correspondence of the added topographic details, we extracted the highpass components of the photoclinometric result and computed its proportionality with that of the reference DEM. The highpass proportionality coefficient (HPC) of ideal shape correspondence would yield (HPC = 1). The highpass components were obtained by subtracting the DEMs from their lowpass filtered version. Here we used a 75 m × 75 m boxcar averaging kernel for lowpass filtering, echoing the resolution of the HRSC DEM. The computed proportionality measure ($HPC_{75} = 1.04$) is close to unity, which is desirable since the highpass components at this scale had similar geometric shapes.

The scale variations of RMS deviations were computed based on 5 m spatial resolution. Therefore, all the DEMs were first interpolated to 5 m/pixel. The results were plotted in Fig. 10 to allow evaluation of how RMS deviations of the DEMs change over scales. The green crosses indicate that the photoclinometric DEM has reached minimal RMS deviation (10.471 m) when the reference DEM is smoothed by a boxcar of width $k \approx 55$ pixels (~275 m), while the HRSC DEM has its minimal RMS of 11.908 m when the reference DEM is smoothed by a boxcar of $k \approx 200$ pixels (~1000 m). The RMS curve for the photoclinometric result (blue line) has indicated a significant improvement over the HRSC DEM (red line) at all finer scales until approximately $k \approx 200$ pixels, where the

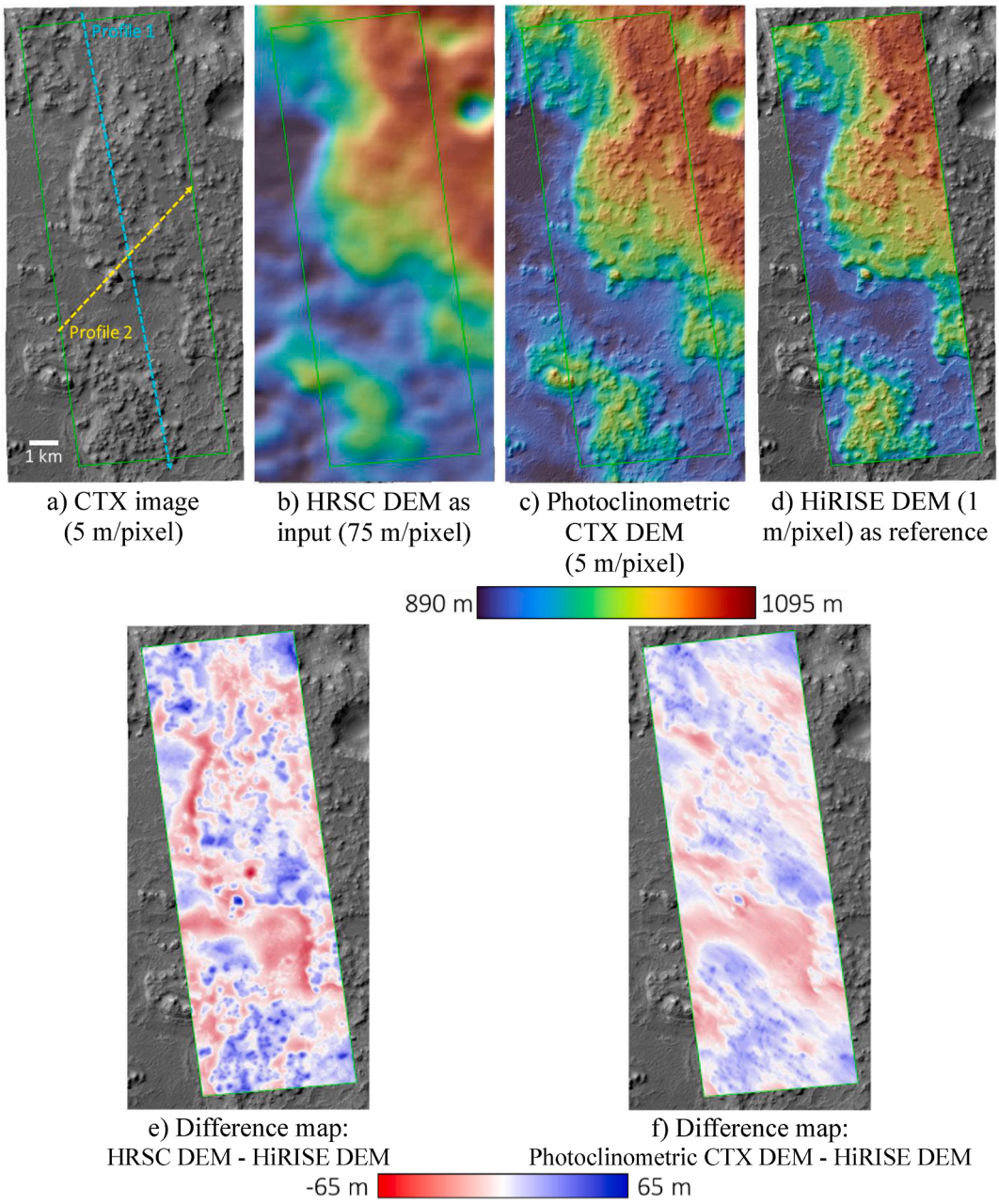

Fig. 9. Photoclinometric results of the CTX dataset.

Table 5
Information of the input CTX image (ID: J01_045278_1498_XN_30S165W).

Acquisition time	2016-03-24T13:08:24.377				
Optical depth (from MCD)	0.11	Resolution (m/pixel)	5	Sub-solar azimuth (°)	316.58
Angle of incidence (°)	70.66	Angle of emission (°)	30.0	Phase angle (°)	51.75

Table 6
Overall quality metrics of the CTX dataset.

	HRSC DEM (75 m/pixel)	Photoclinometric CTX DEM (5 m/pixel)	HiRISE DEM as reference (1 m/pixel)
RMSE (m)	15.7	11.0	N/A
Max. Abs. (m)	63.8	47.0	N/A
PCC_{img}	0.215	0.950	0.887

*PCC_{img} is the Pearson correlation coefficient of the computed shaded relief and input image.

photoclinometric DEM remains a similar but slightly higher (less than 0.5 m) RMS than the HRSC DEM. The RMS increase found in scales $k \leq 55$ pixels can be interpreted as a decrease in signal-to-noise ratio (SNR): Photoclinometry adds topographic details to the DEM but also introduces uncertainties. At finer scales, the proportion of noise added to the result increases slightly, as indicated by the small RMS increase (~6 % at pixel scale, $k = 1$), hence having a reduced SNR.

Fig. 11 presents the cross-sections of two profiles depicted in Fig. 9a. The first profile passed through the region across the NE-SW direction, which enabled the assessment of the overall reconstructed topography. The local topographic features, including craters and depressions of as large as ~50 m, were missing in the HRSC DEM (red dashed lines). These

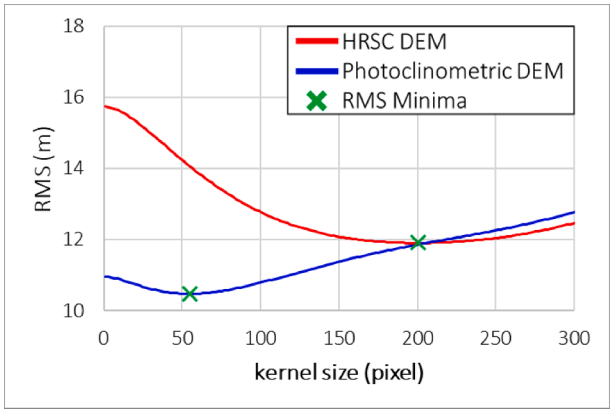

Fig. 10. DEM RMS at different scales for the CTX dataset.

features were successfully reconstructed in the photoclinometric CTX DEM (blue lines), with high correspondence with the HiRISE DEM (green dotted lines).

The second profile in Fig. 11 ran approximately along the cross-Sun direction across the region. This profile enabled the assessment of the performance of our approach along directions perpendicular to illumination, which is one of the known limitations in single-image photoclinometry (Liu et al., 2021). The result indicates that the approach successfully reconstructed the three bulges not captured by the input HRSC DEM. The reconstructed profile exhibited high correspondence with the reference HiRISE DEM, indicating that our approach is effective along the cross-Sun direction.

Here we also report the time used to compute our experimental datasets. The 3D reconstruction processes of the three experimental datasets required from 0.5 h (for the HiRIC image of 2711 × 3809 pixels and CTX image of 1576 × 3142 pixels) to approximately 1 h (for the HiRISE image of 5177 × 6856 pixels) on an ordinary computer (running Windows 11 and equipped with a 4-core CPU of 3.2 GHz and 16 GB RAM, without using the GPU).

5. Extended analysis

5.1. Comparison with the linear approximation method

5.1.1. Model comparison

The described TOA model (Eq. (1)) is compared with a linear approximation of the kind $\{aR_{dd} + b\}$ where a and b are respectively the scale and offset parameters that linearly transform R_{dd} to fit I_{TOA}. The linear approximation method is simple and does not require an RTM, hence often being selected to account for the atmospheric scattering effects. The goal of this comparison is to understand the fitness of the linear method in approximating the more sophisticated TOA model. We computed I_{TOA} and its corresponding linear approximation for a range of practical settings of Mars satellite images. The specific settings were summarised in Table 7. The albedo ω is normalised to 1 so that $a = 1$ when $\tau = 0$, setting $\omega \neq 1$ linearly affects the parameter a and the absolute deviation of the fitted line. On the other hand, the relative fitness of the line, such as correlation and relative deviation, is not affected. We only included pairs of (I_{TOA}, R_{dd}) in the linear fitting where $R_{dd} > 0$ (i.e., sun-lit surfaces). A few such fittings were exemplified in Fig. 12. It is trivial to notice the linear distributions of the samples and how the slopes flatten (implying a decrease in contrast) as τ increases. Further,

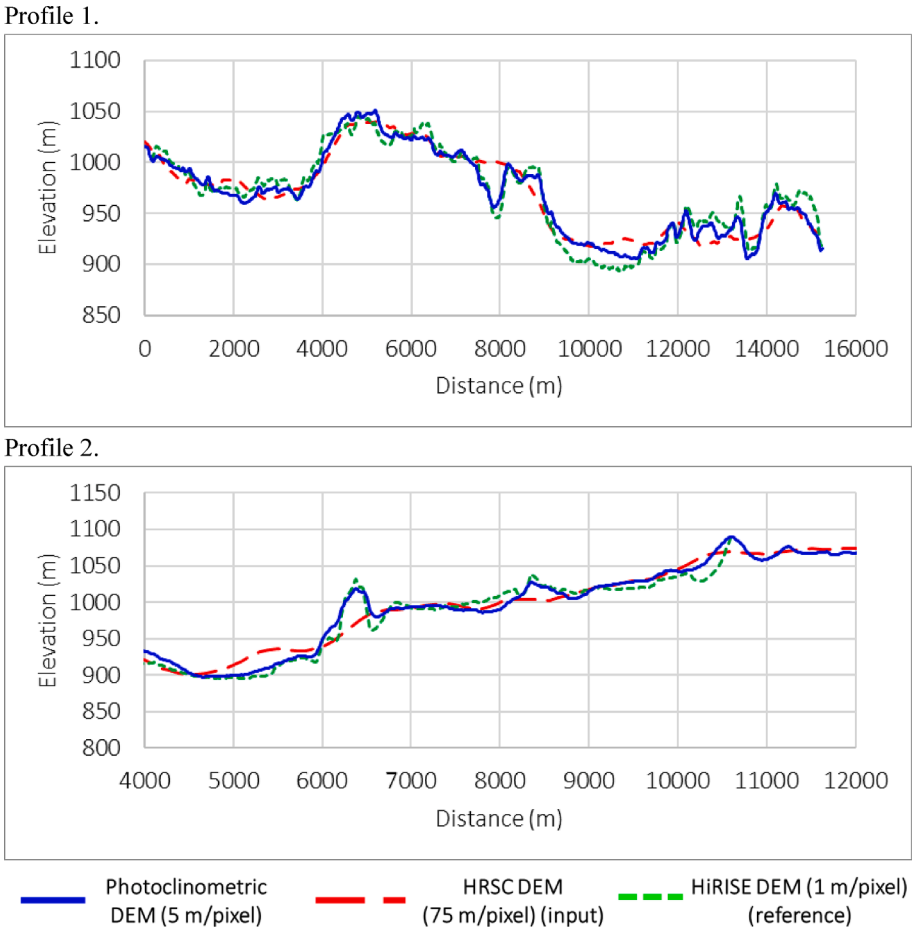

Fig. 11. Selected topographic profiles of the CTX dataset.

Table 7
Settings used to compute I_{TOA} and R_{dd}.

Incidence angle	40°, 50°, 60°
Topographical slopes	−80° ≤ x slopes ≤ 80° −80° ≤ y slopes ≤ 80°
Emission angle	0°
Optical depth	0 ≤ τ ≤ 2

because of the atmospheric scattering, the I_{TOA} of self-shadowed surfaces (red crosses in Fig. 12) still contain limited information and are thus not constant, resulting in a deviation from parameter *b*.

The linear fitting results were summarised in Table 8 and plotted in Fig. 13. As expected, the approximations were highly linear: Most of the R^2 values were above 0.9, except the cases for 60 incidence angle at τ > 1.6, where R^2 values were still greater than 0.8. For all scenarios, the parameters *a* and *b* (Fig. 13a and b) changed monotonically with τ. Scenarios with greater incidence angles have parameter *a* dropping more quickly (i.e., fitted lines flattened faster) as τ increases, possibly due to a longer optical path. In contrast, parameter *b* increases more slowly with τ for greater incidence angles. The absolute deviations are presented in Fig. 13(c), for each incidence angle, the absolute deviation first increases and then decreases as a function of τ. Cases with higher incidence angles have smaller overall deviations and their peak deviation was found at smaller τ. The peak deviations for all cases were found at τ ≤ 0.5 in this test.

Since the photometric contrast produced by topography decreases with τ, as can be seen by the flattening of linear approximations, the same amount of deviation may constitute a greater relative deviation. Therefore, in Fig. 13(d), we normalised the absolute deviation by the value range of I_{TOA} samples (i.e., max(I_{TOA}) – min(I_{TOA})) to understand the deviations relative to photometric contrast. The results follow a non-monotonic yet generally increasing trend with τ. Relative deviations for higher incidence angles were at first (approximately τ ≤ 0.8) lower than that of lower incidence angles but then gradually catch up and surpass their lower-incidence counterparts. In this test, these surpassing points were all found at τ > 0.8. The 40-incidence case has the highest relative RMS deviation among all for τ ≤ 0.9 and the highest relative max deviation for τ ≤ 1.4, after which the 60-incidence case took over. The 60-incidence case reached 10 % relative RMS and 20 % relative max deviations at τ ≈ 1.8, the earliest of the three, and exceeded thereafter, while the other two cases have their 10% RMS and 20% maximum lines

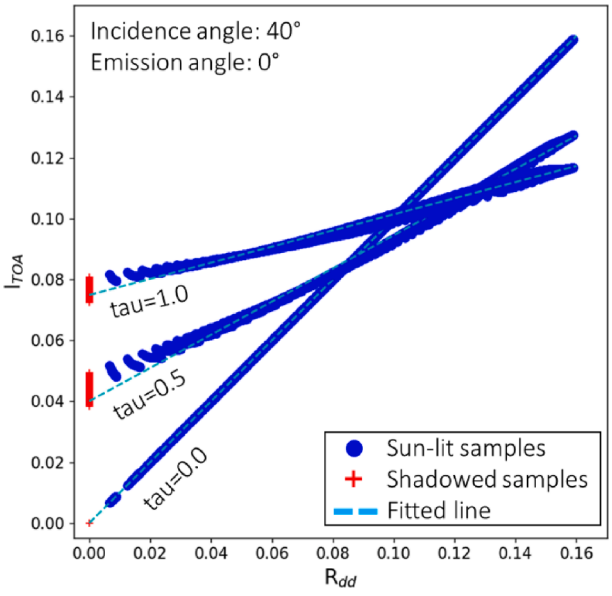

Fig. 12. Examples of linear approximation fitting results.

Table 8
Fitting results of the linear approximation method.

Incidence Angle: 40°, Emission angle: 0°

τ	*a*	*b*	R^2	Abs. RMS (Rel. RMS)	Abs. Max (Rel. Max)
0.0	1	0	1.000	0 (0 %)	0 (0 %)
0.2	0.801898	0.015939	0.999	0.001257 (1.06 %)	0.006641 (5.58 %)
0.4	0.626241	0.032225	0.997	0.001496 (1.63 %)	0.008327 (9.08 %)
0.6	0.477648	0.047514	0.995	0.001419 (2.05 %)	0.007826 (11.33 %)
0.8	0.358099	0.061719	0.993	0.001262 (2.47 %)	0.006512 (12.74 %)
1.0	0.264831	0.074902	0.990	0.001110 (2.98 %)	0.005040 (13.53 %)
1.2	0.193906	0.087181	0.985	0.000980 (3.65 %)	0.003711 (13.83 %)
1.4	0.140819	0.098658	0.978	0.000868 (4.47 %)	0.002621 (13.50 %)
1.6	0.101554	0.109402	0.968	0.000766 (5.43 %)	0.001881 (13.34 %)
1.8	0.072817	0.119422	0.952	0.000670 (6.52 %)	0.001568 (15.26 %)
2.0	0.051981	0.128805	0.932	0.000580 (7.71 %)	0.001293 (17.19 %)

Incidence Angle: 50°, Emission angle: 0°

τ	*a*	*b*	R^2	Abs. RMS (Rel. RMS)	Abs. Max (Rel. Max)
0.0	1	0	1.000	0 (0 %)	0 (0 %)
0.2	0.773616	0.016305	0.999	0.001111 (1.02 %)	0.005527 (5.08 %)
0.4	0.5828	0.033105	0.997	0.001210 (1.49 %)	0.006505 (7.99 %)
0.6	0.429345	0.048523	0.996	0.001075 (1.81 %)	0.005744 (9.67 %)
0.8	0.311273	0.062409	0.995	0.000930 (2.18 %)	0.004466 (10.49 %)
1.0	0.222976	0.074862	0.992	0.000827 (2.75 %)	0.003203 (10.66 %)
1.2	0.158245	0.086071	0.987	0.000754 (3.58 %)	0.002149 (10.22 %)
1.4	0.111426	0.096211	0.978	0.000688 (4.68 %)	0.001715 (11.67 %)
1.6	0.078009	0.105439	0.963	0.000621 (5.94 %)	0.001452 (13.88 %)
1.8	0.054319	0.113855	0.942	0.000551 (7.39 %)	0.001209 (16.19 %)
2.0	0.037651	0.121568	0.911	0.000481 (8.95 %)	0.000997 (18.55 %)

Incidence Angle: 60°, Emission angle: 0°

τ	*a*	*b*	R^2	Abs. RMS (Rel. RMS)	Abs. Max (Rel. Max)
0.0	1	0	1.000	0 (0 %)	0 (0 %)
0.2	0.716631	0.017112	0.999	0.000830 (0.89 %)	0.004080 (4.36 %)
0.4	0.503719	0.034018	0.998	0.000810 (1.24 %)	0.004310 (6.58 %)
0.6	0.348649	0.048608	0.997	0.000701 (1.56 %)	0.003403 (7.58 %)
0.8	0.238819	0.060931	0.995	0.000649 (2.14 %)	0.002318 (7.65 %)
1.0	0.16236	0.071334	0.990	0.000632 (3.08 %)	0.001637 (7.99 %)
1.2	0.109749	0.080210	0.980	0.000609 (4.40 %)	0.001458 (10.51 %)
1.4	0.073836	0.087895	0.962	0.000569 (6.07 %)	0.001258 (13.43 %)
1.6	0.049483	0.094624	0.934	0.000514 (7.95 %)	0.001061 (16.42 %)
1.8	0.033043	0.100590	0.891	0.000452 (9.96 %)	0.000881 (19.44 %)
2.0	0.021994	0.105980	0.830	0.000388 (12.00 %)	0.000757 (23.43 %)

*Rel. RMS and Rel. Max refer to the RMS and Maximum deviations relative to the maximum contrast available by the I_{TOA} samples (i.e., max(I_{TOA}) − min (I_{TOA})).

beyond $\tau = 2$. For convenience, a brief summary of relative deviations for all three cases at particular τ is provided below: At $\tau = 0.5$, the relative RMS deviation is $< 2\%$ and the relative max deviation is $< 11\%$ for all three cases. At $\tau = 1$, the relative deviations are $< 4\%$ (RMS) and $< 14\%$ (maximum), respectively. At $\tau = 1.5$, they are $< 7\%$ and $< 15\%$, respectively. These values can be used as rough references in assessing the potential fitness of the linear approximation method.

Note that our RTM model is considered valid for small optical depth ($\tau \leq 1$), as supported by past references (Vincendon et al., 2007; Liu et al., 2022). Therefore, the specific values of τ should be taken as references instead of hard bounds. Nevertheless, the analysis here improves our understanding of the fitness of the linear model in approximating the more sophisticated I_{TOA} model under various practical scenarios.

5.1.2. Experimental comparison

We tested the linear approximation method by replacing the

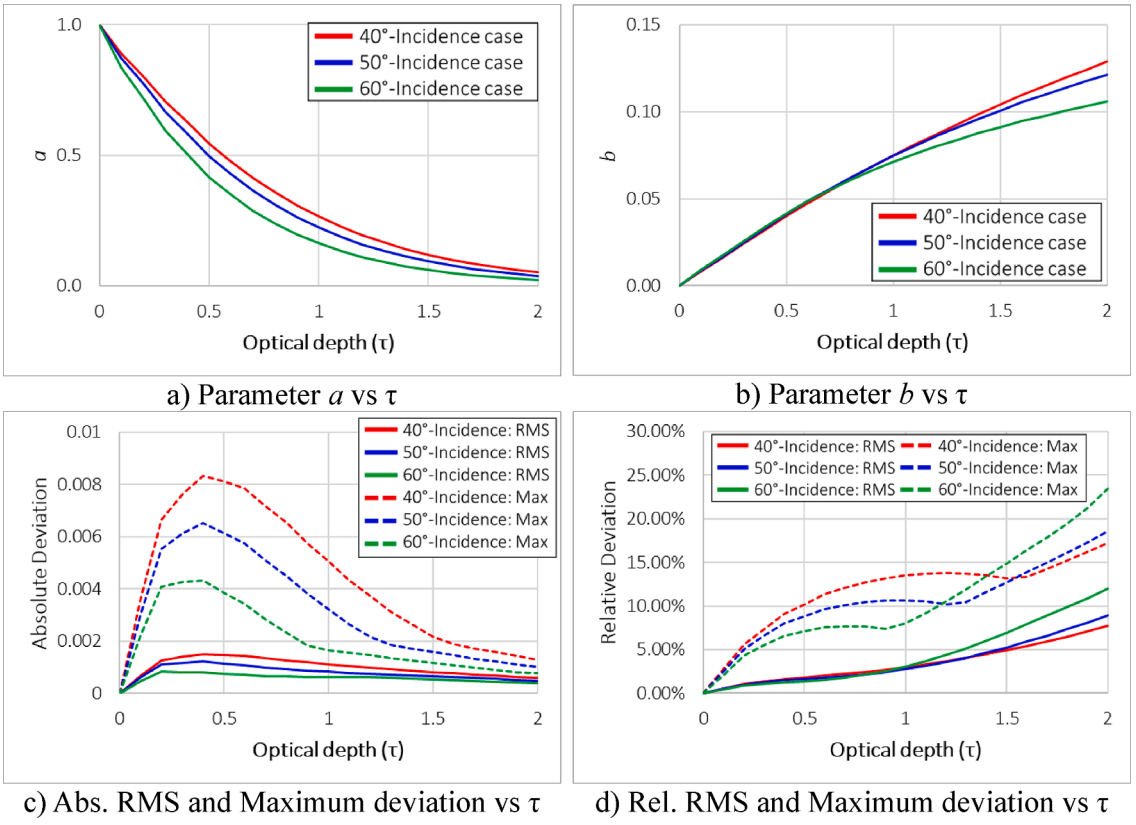

Fig. 13. Fitting results of the linear approximation method.

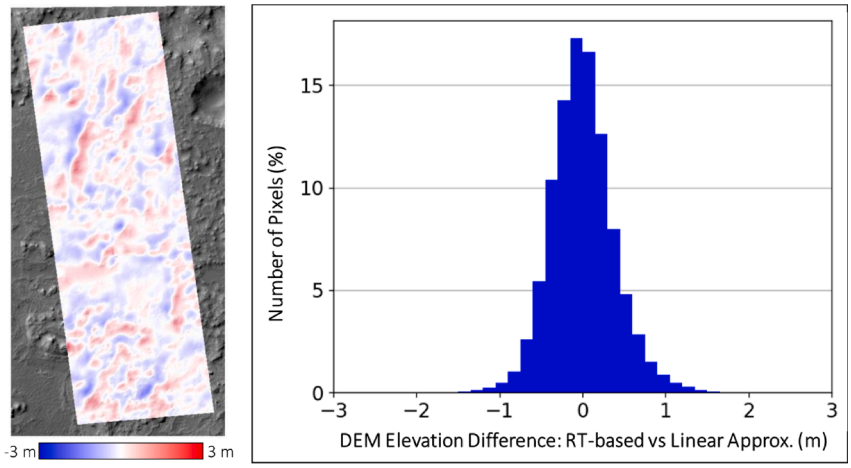

Fig. 14. The Elevation difference between photoclinometric DEM created using the TOA model presented in this paper: "Phcl DEM (RT-based)", and that using a linear approximation method to atmospheric treatment: "Phcl DEM (Linear Approx.)".

radiative transfer-based (RT-based) TOA model in Eq. (1) with the linear model $\{aR_{dd} + b\}$. The scale parameter a is considered as 'albedo' that will be optimised within the system whereas the offset parameter b is obtained by averaging pixel values within shadows. We used the Columbus crater dataset in section 4.3 to perform this test since we believe it has the most reliable reference DEM among all. By averaging shadowed pixel values we obtained $b = 0.0167$ for this dataset. The results are shown in Fig. 14, for clarity only the elevation difference between the two photoclinometric DEMs was presented. From section 5.1.1 one would expect similar photoclinometric results. This is supported experimentally by the limited amplitudes: the difference between the two photoclinometric DEMs ranges from −1.52 m to 2.05 m, with the RMS deviation of 0.378 m. The histogram in Fig. 14(b) showed that the elevation differences can be considered normally distributed. The difference map (Fig. 14a) did not show signs of systematic patterns. An overlay with the original CTX image would find that the linear approximation method resulted in steeper slopes, deeper craters and higher bulges. From the later section 5.2, the greater amplitudes of local landforms might imply that the chosen parameter b might correspond to a higher optical depth ($\tau > 0.11$) than that of the RT-based model. The result based on the linear approximation model has an RMS deviation with the reference DEM of 11 m, similar to that based on the proposed RT-based model. The scale variations of RMS plotted in Fig. 15 showed similar trends with the RT-based model but with a larger RMS from $k \approx 13$. Its optimal RMS is 10.5 m when $k \approx 50$.

This test showed that photoclinometry based on the RT-based and the linear approximation models produced similar results, which is reasonable since the dataset's optical depth is low ($\tau = 0.11$ according to the MCD). Larger differences are expected when the atmosphere is more opaque (larger τ) but extra tests are needed to confirm and quantify the differences. Using the linear method provides a quick treatment for atmospheric effects. However, the offset value (normally from shadowed pixels) has to be chosen carefully since pixel values might vary considerably with the choice of shadows (Liu et al., 2022). Also, its connection with optical depth is less intuitive since the model is further simplified. Using the proposed RT-based TOA model, on the other hand, allows for a more intuitive treatment since the TOA model is directly related to optical depth. It also allows for directly adopting optical depth values from external sources, such as the MCD. Moreover, the test also indicates that the proposed photoclinometric approach can be applied to both more sophisticated and simplified models, which offers flexibility in actual applications.

5.2. Effects of optical depth on the reconstructed DEMs

5.2.1. Analysis based on rover measurements

We evaluated the effects of the optical depth by using the HiRISE dataset at the Victoria Crater (Section 4.1), because its optical depth has been measured by the Opportunity rover at the same date of the HiRISE image acquisition (Hoekzema et al., 2011; Lemmon et al., 2015). We used the photoclinometric approach to create DEMs with different optical depths. Next, we considered the optical depth measured by the Opportunity rover ($\tau = 0.43$) and the resulting photoclinometric DEM as a reference, the elevation differences between which we considered as errors. The value of the optical depth varied from the underestimation scenario ($0.0 \leq \tau < 0.43$) to the overestimation scenario ($0.43 < \tau \leq 0.8$). The optical depth was overestimated to a limit such that $\alpha(\tau) \leq$ [minimum I_{TOA} of the image]. Exceeding this limit led to negative pixel values when $\alpha(\tau)$ was subtracted from the image, resulting in increased errors. The limit of optical depth for the HiRISE dataset was approximately 0.8, and therefore we did not analyse situations with $\tau > 0.8$.

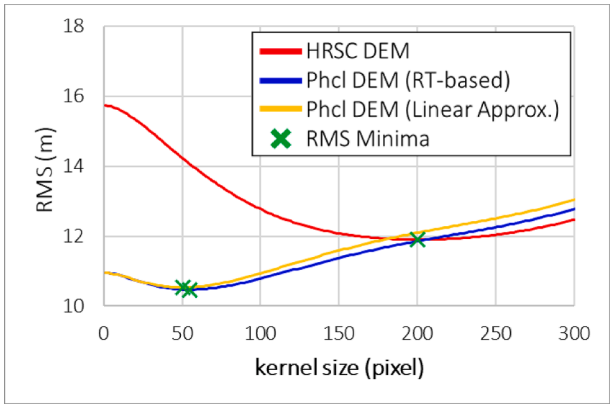

Fig. 15. DEM RMS at different scales for the CTX dataset with the results based on linear approximation method included.

In Fig. 16 we visualised the topographic cross-sections estimated under a range of τ. One would notice that the topography created from an underestimated optical depth (e.g., $\tau = 0.0$, red dashed lines) results in an underestimation of topographic amplitudes, hence leading to such situations as shallower craters and flatter boulders. In contrast, the cross-section created from an overestimated optical depth (e.g., $\tau = 0.8$, green dashed lines) results in greater topographic amplitudes, such as steeper slopes, deeper craters and taller boulders. This might have been because overestimating the optical depth led to a larger $\alpha(\tau)$, which increased the contrast between the image pixels. Therefore, the local slopes and resulting DEM were exaggerated.

To better understand how the topographic amplitudes change with optical depth, we extracted the highpass components of the DEMs. This is realised by subtracting from each DEM a Gaussian smoothed version of itself. The sigma of the Gaussian smoothing kernel is set as $32/6 \approx 5.33$ pixels, approximately corresponding to the initial resolution of 8 m. We then analysed the level of over- or underestimation and plotted the results in Fig. 17. The plot exhibits an exponential pattern, which may correspond to the atmospheric attenuation factors (exponential functions of τ) in Eq. (1). Increasingly underestimating optical depth yielded a gentler increase in underestimation of topographic amplitudes, whereas overestimating the optical depth by the same amount typically resulted in a greater overestimation. This is also observed in Fig. 16, where results from overestimation are more deviated from the reference than that from underestimation. These results highlight that if the optical depth of an image is unknown, it is preferable to use a smaller value if only the overall accuracy needs to be maintained. However, for applications such as landing site assessments where steep slopes would pose extra risks to landing, a reasonable overestimation might be appropriate so as not to overlook potential risks. For reference, the errors in optical depths provided by the MCD can be up to 50 % (Montabone et al., 2015), the corresponding bounds at ±50 % were marked in Fig. 17 (grey band). For this particular dataset, a 50 % underestimation of τ results in an underestimation of topography by up to 26 % (e.g., the crater depths would be 26 % shallower), while a 50 % overestimation of τ corresponds to an overestimation of topography by up to 48 %. Note that in practice, the errors in topographic amplitudes are affected by illumination and imaging geometries, actual optical depth, and the initial DEM available. The results presented here serve as an example to illustrate the general behaviour. In addition, because the atmospheric RTM is configured for small τ ($\tau < 1$) (Petrova et al., 2012), this implication is expected to hold for images with a clear sky. Nevertheless, a comprehensive test involving various optical depths must be performed to assess the universality of the implication, especially for images with large optical depths, because they have more room for underestimation than those with small optical depths.

5.2.2. Analysis based on estimates from the MCD model

We further analyse the effects of optical depth using the CTX dataset for the Columbus Crater where a reliable reference DEM is available. We created photoclinometric DEMs based on optical depths $\tau = 0.11$, 0.2 and 0.3, respectively. Following Kirk et al. (2022), the scale variations of

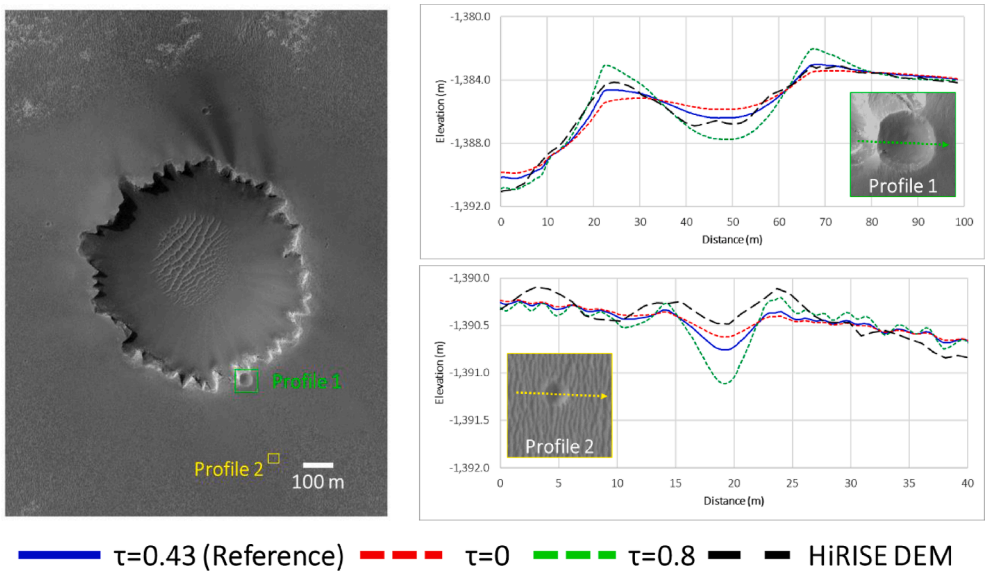

Fig. 16. Selected topographic profiles from the experimental results.

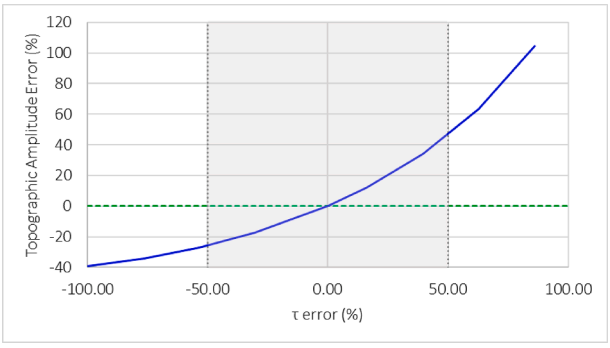

Fig. 17. Scale error of topographic amplitude produced by photoclinometry under different optical depths (the reference optical depth was set as $\tau = 0.43$). The grey band indicates a ±50 % error in optical depth. The green dashed line indicates the line of zero error.

RMS deviations of each photoclinometric result are plotted in Fig. 18. The results showed that the RMS deviations for $\tau = 0.11$ and 0.2 were very close at fine scales ($k \leq 20$). Afterwards, the result for $\tau = 0.2$ has visibly higher RMS deviations than that of $\tau = 0.11$. Nevertheless, such deviations do not exceed 2.3 m. The case for $\tau = 0.3$ has the highest RMS deviation for all scales analysed. It differed from the rest by at least 3.7 m and isolated, an apparent sign of unreasonable optical depth. The curves suggest that the best optical depth estimate should be close to $\tau = 0.11$ and 0.2.

At pixel resolution (5 m) the RMS deviation relative to the reference HiRISE DEM is 10.96 m for $\tau = 0.11$, 10.85 m and 14.57 m for $\tau = 0.2$ and 0.3, respectively. We then estimated the optimal optical depth by applying a least-squares approach on the three RMS values and yielded $\tau \approx 0.158$, about 44 % higher than the estimate from MCD ($\tau = 0.11$), within the reported uncertainties of ±50 %. We performed such estimation for each scale k and the optimal optical depths were plotted in Fig. 19 (blue line). For reference, the MCD estimate $\tau = 0.11$ was also overlaid on the plot (black dashed line). The results showed that the optimal τ is monotonically decreasing with scale k (i.e., finer scales suggest higher τ while coarser scales suggest lower). This suggests that fine-scale topography is more sensitive to optical depth than coarser scales, which we believe is reasonable since the reconstruction of fine-scale topography relies almost solely on photoclinometry. At coarser scales, the DEMs are smoother (lower topographic amplitudes) and thus favoured lower optical depths. From this test, choosing a specific value for τ would favour reconstruction quality at a certain scale at the expense of other scales. If the pixel-wise topography is of concern, then estimates based on higher resolution should be appropriate. Nevertheless, if the choice for τ is within a reasonable range, photoclinometric results are unlikely to deviate from each other drastically, although RMS

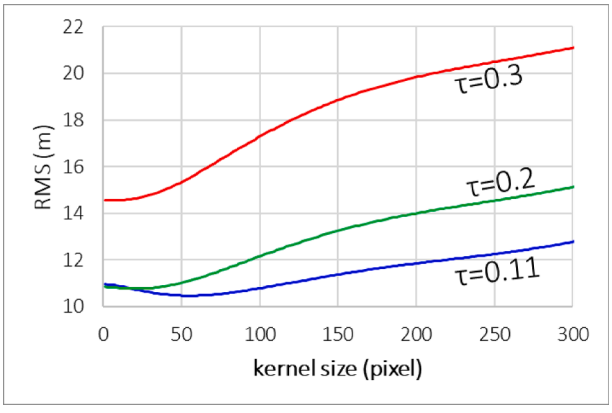

Fig. 18. Scale variations of RMS deviation relative to the reference HiRISE DEM.

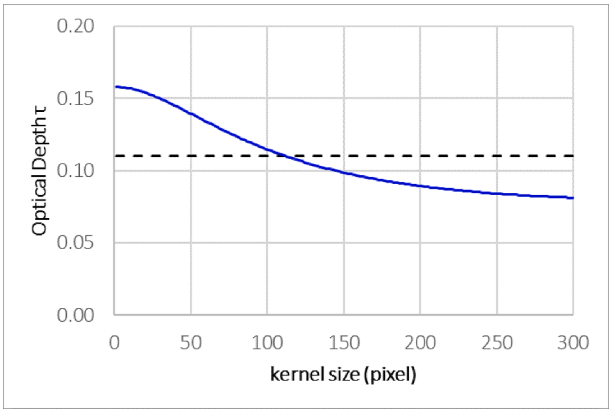

Fig. 19. Optical depths estimated using RMS deviations at multiple scales.

deviation at specific scales may vary.

5.3. Effects of spatial resolutions of the initial DEMs

Next, we attempted to clarify the effects of the spatial resolution of the input DEM on the photoclinometric results. The test was performed using the CTX dataset for the Columbus Crater (Section 4.3) because the reference HiRISE DEM (1 m/pixel) has sufficient resolution to provide quality assessments. It is important to note that the actual errors resulting from photoclinometry can be affected by a range of factors (Jankowski & Squyres, 1991; Wu et al., 2018; Kirk et al., 2021, 2022; Liu & Wu, 2021), such as illumination and imaging conditions, the relief characteristics of the area of interest, variations in surface albedo, and other prior information available (e.g., photometric model, initial DEM). Therefore, this experimental test serves as an example of an overall behaviour. The exact values resulting from the test (e.g., RMSE, resolutions) should be interpreted with care. We first down-sampled the HiRISE DEM into a set of predefined spatial resolutions: 25, 50, 100, 200 and 400 m/pixel, which are equivalent to 5, 10, 20, 40, and 80 grid spacing with respect to the CTX image resolution (5 m/pixel), respectively. These down-sampled HiRISE DEMs were used as inputs to the photoclinometric approach, and the resulting DEMs (5 m/pixel) were compared with the original reference HiRISE DEM.

Again, following Kirk et al. (2022) we have computed the scale variations of RMSE for different initial resolutions and identified the optimal scales where the RMSE is minimal, as exemplified in Fig. 20(a). The results were summarised in Table 9 and plotted in Fig. 20(b). For all initial resolutions, the optimal scale k identified on the photoclinometric DEMs is lower than that of their initial DEMs. Such reductions in optimal scale are signs of improvements in spatial resolutions and topographic details. At a 5-pixel initial resolution, the improvement is about 22%, the improvements then increased with the initial resolution. At the 80-pixel initial resolution case, the improvement is up to about 73%. On the other hand, the RMSE of photoclinometry DEMs at optimal scales were higher than that of the initial DEMs. We believe this is reasonable since photoclinometric DEMs have incorporated the information provided by and the uncertainties inherited from the image and the technique, while the initial DEMs are simply smoothed versions of the reference DEM. Nevertheless, from Fig. 20a one could notice the improvements in RMSE at finer scales.

When considering the situation at pixel scale, as summarised in Table 10 and plotted in Fig. 21. Both initial DEMs' and photoclinometric DEMs' RMSE increased monotonically relative to the initial resolution.

Table 9
Optimal smoothing kernel size (k) and corresponding RMSEs with different initial grid spacings.

Initial Resolution / Grid spacing (pixel/grid)	Initial DEM		Photoclinometry DEM	
	Optimal k (pixel)	RMSE at optimal k (m)	Optimal k (pixel)	RMSE at optimal k (m)
5	10.67	0.103	8.33	0.494
10	21.25	0.195	15.87	0.981
20	42.10	0.435	24.48	1.981
40	82.22	0.881	35.59	3.724
80	161.53	1.475	43.85	6.412

However, the RMSE values decreased after photoclinometry as compared with the initial DEMs', except for the slight increase when the initial resolution was 5-pixel. In addition, compared with the photoclinometric DEMs using finer initial resolutions, those using coarser initial resolutions resulted in a larger reduction in the RMSE. This trend became generally stable when the initial resolution reached 40 pixels (200 m), the reduction then fluctuated at approximately 30%. We then examined the error map of the 400 m/pixel (i.e., 80 pixels coarsened) initial DEM in Fig. 22(a) to understand the spatial patterns of the errors. We found that most of the significant errors are bulges and pits (e.g., craters) of size ranging approximately from 100 m to 400 m. We proceeded to apply SIFT (Lowe, 2004) on the error map and extracted 1021 keypoints. We then summarised the size distribution of these keypoints in Fig. 22(b), which helps us to briefly understand the size distribution of the error patches. The results showed that error patches of size 10–40 pixels constitute almost 85% of all detected error patches, while errors ≤10 pixels and >40 pixels in diameter constitute less than 11% and 5% of the population, respectively. The statistical findings may have

Table 10
RMSE of input DEM and photoclinometric results with different initial grid spacing.

Initial Resolution/ Grid spacing (pixel/grid)	Initial RMSE at pixel-scale (m)	Photoclinometry RMSE at pixel-scale (m)	RMSE reduction at pixel-scale
5	0.63	0.66	3.9 %
10	1.47	1.34	−9.0 %
20	3.25	2.47	−23.8 %
40	6.20	4.34	−30.1 %
80	9.68	6.93	−28.4 %

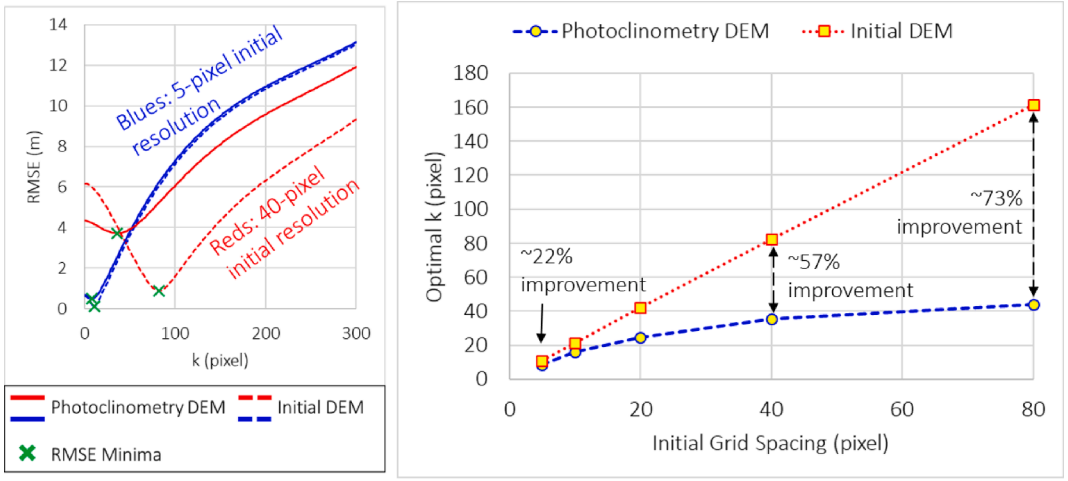

a) Examples of scale variations of RMSE

b) Optimal smoothing kernel size of the DEMs

Fig. 20. Optimal smoothing kernel size of the DEMs at different initial grid spacing (values are summarised in Table 9).

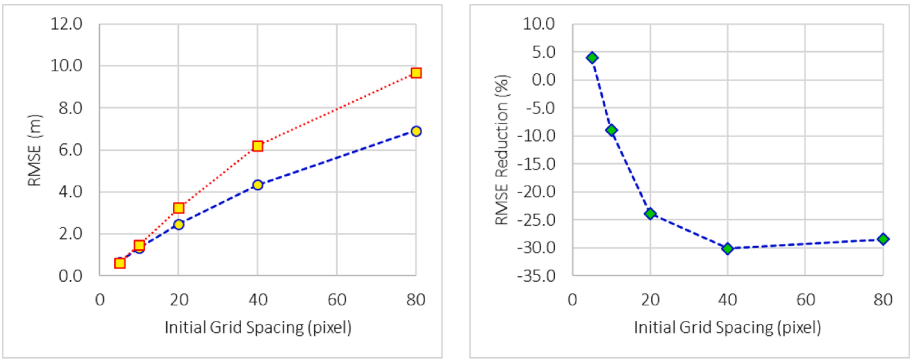

a) RMSE values of initial and photoclinometric DEMs

b) Decrease in the RMSE after photoclinometry

Fig. 21. Plot of RMSEs of DEMs and decrease in the RMSE after photoclinometry with the initial grid spacing (values are summarised in Table 10).

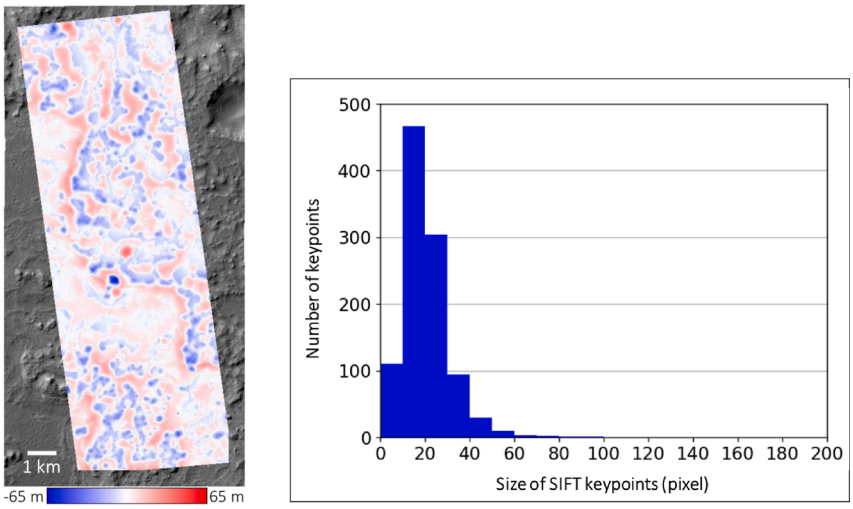

a) Error map of the initial DEM (400 m/pixel)

b) Size Distribution of SIFT keypoints detected in (a)

Fig. 22. The error map of the initial DEM (400 m /pixel) and the size distribution of the detected SIFT keypoints. The total number of SIFT keypoints is 1021.

provided clues to explain the stable RMSE improvements when the initial resolution (grid spacing) exceeds 40 pixels: when the initial DEM is coarsened to 40 times the original, most of the significant local topographies were removed. Therefore, further coarsening of the initial DEM did not further remove local topography significantly, but only flattened the overall terrain. As a result, the improvements that can be made by photoclinometry become stable when the initial resolution reaches 40 pixels for this particular dataset. Further increment in initial resolution (e.g., from 40-pixel to 80-pixel grids) may in turn lead to a steady increase in actual RMSE due to the weakening of the DEM constraint and the flattening of overall terrain by the input DEM. These results highlight that the "critical initial resolution" where photoclinometry may reach its improvement limit depends likely on the terrain of the region of interest, such as the size distribution of landforms, and also the size distribution of the errors of the input DEM, which is related to the input DEM's effective spatial resolution. In practice, one could infer the size distribution of landforms by inspecting the image, or by using image-based feature detection methods (e.g., crater detection). The effective spatial resolution of the input DEMs can be analysed by the method explained in Kirk et al. (2022), which is also used in this paper. Another way would be to infer by inspecting the sizes of resolvable landforms in the DEM. Understanding these properties would help create realistic expectations on the extent photoclinometry will be useful for particular studies, thereby maximising the potential of the technique in scientific applications.

6. Conclusions and discussions

This paper presents an atmosphere-aware photoclinometric approach for pixel-wise 3D mapping of the Martian surface. The approach takes a high-resolution image and a corresponding coarse-resolution DEM as inputs to produce a pixel-wise high resolution DEM. It incorporates a radiative transfer model to describe the unique photometric behaviour of the Martian atmosphere, thereby allowing consideration of the non-uniform skylight of Mars. The time-varying atmospheric parameter required by the approach, optical depth, can be obtained by the globally available MCD (Montabone et al., 2015) or image-based methods (Hoekzema et al., 2011; Liu et al., 2022). The approach was evaluated using images collected by the HiRISE, CTX, and HiRIC. The experimental results show that the high-resolution DEMs reconstructed using the photoclinometric approach achieved an overall geometric accuracy (RMSE of the elevation) of approximately 2 pixels of the image resolution. In addition, the approach significantly improved the topographic details of the reconstructed DEMs and their similarity with the input images. Analysis of topographic profiles confirms that the high-resolution surface details were effectively imprinted to the

resulting DEMs.

Moreover, the effects of the optical depth and spatial resolution of the input DEMs on the performance of the approach were evaluated. The results indicate that underestimating optical depth leads to flattened local topography and vice versa for overestimation. Further, the overall RMSE increase for overestimation is higher than that of an underestimation of optical depth by the same amount. This is potentially because the topographic exaggeration resulting from an overestimation yielded larger topographic deviations than those resulting from an underestimation. This implication is expected to hold for images obtained in clear sky conditions (optical depth < 1), considering the datasets used and configured atmospheric RTM. Further testing is required to ensure scalability over higher optical depths. Regarding the effects of spatial resolution, the RMSE monotonically increased with the coarsening of the input DEMs. Nevertheless, photoclinometry improved the overall resolution and RMSE of the input DEMs. A turning point is identified where the ratio of improvements becomes stable even when the input DEM is further coarsened. This turning point is likely related to the size distribution of the features in the area and the spatial quality of the initial DEM (e.g., effective spatial resolution). It is important to emphasise that the actual error in photoclinometry is affected by a multitude of factors: illumination and imaging geometry, relief and albedo characteristics of the region, quality of the input image and DEM, etc. The tests provided here serve as examples to demonstrate the overall patterns.

The developed atmosphere-aware photoclinometric approach provides an effective solution for applying photoclinometry to the pixel-wise 3D topographic mapping of Mars, which will have great potential for exploiting the large amount of high-resolution monocular images of Mars for 3D topographic mapping. Our additional tests provide insights into the performance characteristics of the approach and, to a broader extent, the class of methods used in planetary photoclinometry. Further research can be aimed at extending our approach to enable automated large-scale pixel-resolution 3D mapping of Mars.

Declaration of Competing Interest

The authors declare that they have no known competing financial interests or personal relationships that could have appeared to influence the work reported in this paper.

Acknowledgements

This work was supported by grants from the Research Grants Council of Hong Kong (RIF Project No: R5043-19, CRF Project No: C7004-21GF, Project No: PolyU 15210520, Project No: PolyU 15215822). The HiRISE and CTX images are available in Mars Orbital Data Explorer (https://ode.rsl.wustl.edu/mars/). The authors would like to thank all those who worked on the archive of the datasets to make them publicly available.

References

Alexandrov, O., Beyer, R.A., 2018. Multiview shape-from-shading for planetary images. Earth Space Sci. 5, 652–666.
Barker, M.K., Mazarico, E., Neumann, G.A., Smith, D.E., Zuber, M.T., Head, J.W., 2021. Improved LOLA elevation maps for south pole landing sites: Error estimates and their impact on illumination conditions. Planet. Space Sci. 203, 105119.
Barron, J.T., Malik, J., 2011. High-frequency shape and albedo from shading using natural image statistics, in: CVPR 2011. Presented at the 2011 IEEE Conference on Computer Vision and Pattern Recognition (CVPR), IEEE, Colorado Springs, CO, USA, pp. 2521-2528.
Bell III, J.F., Malin, M.C., Caplinger, M.A., et al., 2013. Calibration and Performance of the Mars Reconnaissance Orbiter Context Camera (CTX). International Journal of Mars Science and Exploration 8, 1–14.
Bell, J.F., Maki, J.N., Alwmark, S., et al., 2022. Geological, multispectral, and meteorological imaging results from the Mars 2020 Perseverance rover in Jezero crater. Sci. Adv. 8, eabo4856.
Bertsatos, I., Makris, N.C., 2010. Statistical biases and errors inherent in photoclinometric surface slope estimation with natural light. Icarus 208, 798–810.
Beyer, R.A., 2017. Meter-scale slopes of candidate insight landing sites from point photoclinometry. Space Sci. Rev. 211, 97–107.
Beyer, R.A., Kirk, R.L., 2012. Meter-scale slopes of candidate MSL landing sites from point photoclinometry. Space Sci. Rev. 170, 775–791.
Beyer, R.A., McEwen, A.S., Kirk, R.L., 2003. Meter-scale slopes of candidate MER landing sites from point photoclinometry. J.-Geophys.-Res. 108.
Carsten, J., Rankin, A., Ferguson, D., et al., 2007. Global Path Planning on Board the Mars Exploration Rovers. In: 2007 IEEE Aerospace Conference. Presented at the 2007 IEEE Aerospace Conference, IEEE, Big Sky, MT, USA, pp. 1-11.
Ceamanos, X., Douté, S., Fernando, J., et al., 2013. Surface reflectance of Mars observed by CRISM/MRO: 1. Multi-angle Approach for Retrieval of Surface Reflectance from CRISM observations (MARS-ReCO). J. Geophys. Res. Planets 118, 514–533.
Chen, H., Hu, X., Glaser, P., et al., 2022. CNN-based large area pixel-resolution topography retrieval from single-view LROC NAC images constrained with SLDEM. IEEE J. Sel. Top. Appl. Earth Observat. Rem. Sens. 15, 9398–9416.
Chen, Z., Wu, B., Liu, W.C., 2021. Mars3DNet: CNN-based high-resolution 3D reconstruction of the Martian surface from single images. Remote Sens. (Basel) 13, 839.
Chen-Chen, H., Pérez-Hoyos, S., Sánchez-Lavega, A., 2019. Characterisation of Martian dust aerosol phase function from sky radiance measurements by MSL engineering cameras. Icarus 330, 16–29.
Davis, P.A., Soderblom, L.A., 1984. Modeling crater topography and albedo from monoscopic Viking Orbiter images: 1. Methodology. J. Geophys. Res. 89, 9449.
Doute, S., Ceamanos, X., 2010. Retrieving Mars aerosol optical depth from CRISM/MRO imagery, in: 2010 2nd Workshop on Hyperspectral Image and Signal Processing: Evolution in Remote Sensing. Presented at the 2010 2nd Workshop on Hyperspectral Image and Signal Processing: Evolution in Remote Sensing (WHISPERS), IEEE, Reykjavik, Iceland, pp. 1-4.
Fairbairn, M.B., 2005. Planetary photometry: The Lommel-Seeliger law. J. R. Astron. Soc. Can. 99, 92–93.
Fernando, J., Schmidt, F., Pilorget, C., Pinet, P., Ceamanos, X., Douté, S., Daydou, Y., Costard, F., 2015. Characterization and mapping of surface physical properties of Mars from CRISM multi-angular data: Application to Gusev Crater and Meridiani Planum. Icarus 253, 271–295.
Fernando, J., Schmidt, F., Douté, S., 2016. Martian surface microtexture from orbital CRISM multi-angular observations: A new perspective for the characterization of the geological processes. Planet. Space Sci. 128, 30–51.
Frankot, R.T., Chellappa, R., 1988. A method for enforcing integrability in shape from shading algorithms. IEEE Trans. Pattern Anal. Machine Intell. 10, 439–451.
Gaskell, R.W., Barnouin-Jha, O.S., Scheeres, D.J., et al., 2008. Characterizing and navigating small bodies with imaging data. Meteorit. Planet. Sci. 43, 1049–1061.
Gehrke, S., 2008. Geometric and radiometric modeling of the martian surface based on object space matching and photoclinometry. In: The International Archives of the Photogrammetry, Remote Sensing and Spatial Information Sciences XXXVII-B4, pp. 1031–1036.
Goudge, T.A., Milliken, R.E., Head, J.W., et al., 2017. Sedimentological evidence for a deltaic origin of the western fan deposit in Jezero crater, Mars and implications for future exploration. Earth Planet. Sci. Lett. 458, 357–365.
Grumpe, A., Belkhir, F., Wöhler, C., 2014. Construction of lunar DEMs based on reflectance modelling. Adv. Space Res. 53, 1735–1767.
Gwinner, K., Scholten, F., Spiegel, M., Schmidt, R., Giese, B., Oberst, J., Heipke, C., Jaumann, R., Neukum, G., 2009. Derivation and validation of high-resolution digital terrain models from mars express HRSC data. Photogramm. Eng. Remote Sensing 75, 1127–1142.
Hapke, B., 2012. Theory of reflectance and emittance spectroscopy. Cambridge University Press, Cambridge, New York.
Heipke, C., 1992. Integration of Digital Image Matching and Multi Image Shape from Shading. In: Fuchs, S., Hoffmann, R. (Eds.), Mustererkennung 1992, Informatik Aktuell. Springer, Berlin Heidelberg, Berlin, Heidelberg, pp. 186–198.
Henriksen, M.R., Manheim, M.R., Burns, K.N., Seymour, P., Speyerer, E.J., Deran, A., Boyd, A.K., Howington-Kraus, E., Rosiek, M.R., Archinal, B.A., Robinson, M.S., 2017. Extracting accurate and precise topography from LROC narrow angle camera stereo observations. Icarus 283, 122–137.
Hess, M., Wohlfarth, K., Grumpe, A., et al., 2019. Atmospherically compensated shape from shading on the Martian surface: Towards the perfect digital terrain model of Mars. Int. Arch. Photogramm. Remote Sens. Spatial Inf. Sci. XLII-2/W13, 1405–1411.
Hess, M., Wöhler, C., Bhatt, M., et al., 2020. Processes governing the VIS/NIR spectral reflectance behavior of lunar swirls. A&A 639, A12.
Hess, M., Tenthoff, M., Wohlfarth, K., et al., 2022. Atmospheric correction for high-resolution shape from shading on Mars. J. Imaging 8, 158.
Hoekzema, N.M., Garcia-Comas, M., Stenzel, O.J., et al., 2011. Retrieving optical depth from shadows in orbiter images of Mars. Icarus 214, 447–461.
Horn, B.K.P., 1977. Understanding image intensities. Artif. Intell. 8, 201–231.
Horn, B.K.P., 1990. Height and gradient from shading. Int. J. Comput. Vis. 5, 37–75.
Huang, J., Mumford, D., 1999. Statistics of natural images and models, in: Proceedings. 1999 IEEE Computer Society Conference on Computer Vision and Pattern Recognition (Cat. No PR00149). Presented at the Proceedings. 1999 IEEE Computer Society Conference on Computer Vision and Pattern Recognition, IEEE Comput. Soc, Fort Collins, CO, USA, pp. 541-547.
Jankowski, D.G., Squyres, S.W., 1991. Sources of error in planetary photoclinometry. J. Geophys. Res. 96, 20907.
Jiang, C., Douté, S., Luo, B., et al., 2017. Fusion of photogrammetric and photoclinometric information for high-resolution DEMs from Mars in-orbit imagery. ISPRS J. Photogramm. Remote Sens. 130, 418–430.

Kirk, R.L., Barrett, J.M., Soderblom, L.A., 2003a. Photoclinometry made simple…?. In: ISPRS Commission IV Symposium Presented at the Advances in Planetary Mapping 2003, p. 4.
Kirk, R.L., Thompson, K.T., Lee, E.M., 2001. Photometry of the Martian Atmosphere: An Improved Practical Model for Cartography and Photoclinometry, 1874.
Kirk, R.L., Mayer, D.P., Dundas, C.M., et al., 2022. Comparison of digital terrain models from two photoclinometry methods. Int. Arch. Photogramm. Remote Sens. Spatial Inf. Sci. XLIII-B3-2022, 1059-1067.
Kirk, R.L., Howington-Kraus, E., Redding, B., Galuszka, D., Hare, T.M., Archinal, B.A., Soderblom, L.A., Barrett, J.M., 2003b. High-resolution topomapping of candidate MER landing sites with Mars Orbiter Camera narrow-angle images: MER CANDIDATE LANDING SITE TOPOMAPPING. J.-Geophys.-Res. 108.
Kirk, R.L., Howington-Kraus, E., Rosiek, M.R., et al., 2008. Ultrahigh resolution topographic mapping of Mars with MRO HiRISE stereo images: Meter-scale slopes of candidate Phoenix landing sites. J. Geophys. Res. 113, E00A24.
Kirk, R.L., Mayer, D.P., Fergason, R.L., et al., 2021. Evaluating stereo digital terrain model quality at mars rover landing sites with HRSC, CTX, and HiRISE images. Remote Sens. (Basel) 13, 3511.
Kirk, R.L., 1987. III. A Fast Finite-Element Algorithm for Two-Dimensional Photoclinometry. California Institute of Technology.
Korokhin, V., Velikodsky, Y., Shkuratov, Y., et al., 2018. Using LROC WAC data for Lunar surface photoclinometry. Planet. Space Sci. 160, 120–135.
Lee, C.-H., Rosenfeld, A., 1983. Albedo estimation for scene segmentation. Pattern Recogn. Lett. 1, 155–160.
Lemmon, M.T., Wolff, M.J., Bell, J.F., et al., 2015. Dust aerosol, clouds, and the atmospheric optical depth record over 5 Mars years of the Mars Exploration Rover mission. Icarus 251, 96–111.
Li, Z., Wu, B., Liu, W.C., et al., 2021. Integrated photogrammetric and photoclinometric processing of multiple HRSC images for pixelwise 3-D mapping on Mars. IEEE Trans. Geosci. Remote Sensing 1–13.
Li, Z., Wu, B., Liu, W.C., et al., 2022. Photogrammetric processing of Tianwen-1 HiRIC imagery for precision topographic mapping on Mars. IEEE Trans. Geosci. Remote Sensing 60, 1–16.
Liu, J., Li, C., Zhang, R., Rao, W., Cui, X., Geng, Y., Jia, Y., Huang, H., Ren, X., Yan, W., Zeng, X., Wen, W., Wang, X., Gao, X., Fu, Q., Zhu, Y., Dong, J., Li, H., Wang, X., Zuo, W., Su, Y., Kong, D., Zhang, H., 2021. Geomorphic contexts and science focus of the Zhurong landing site on Mars. Nat. Astron 6, 65–71.
Liu, W.C., Wu, B., 2020. An integrated photogrammetric and photoclinometric approach for illumination-invariant pixel-resolution 3D mapping of the lunar surface. ISPRS J. Photogramm. Remote Sens. 159, 153–168.
Liu, W.C., Wu, B., 2021. Influence of solar incidence angle on single-image photoclinometry for precision lunar topographic mapping. ISPRS J. Photogramm. Remote Sens. 182, 208–227.
Liu, W.C., Wu, B., Wöhler, C., 2018. Effects of illumination differences on photometric stereo shape-and-albedo-from-shading for precision lunar surface reconstruction. ISPRS J. Photogramm. Remote Sens. 136, 58–72.
Liu, W.C., Wu, B., Li, Z., et al., 2022. Pre and post-landing atmospheric optical depths at the Zhurong landing site on Mars retrieved using a single-image-based approach. Icarus, 115223.
Lohse, V., Heipke, C., Kirk, R.L., 2006. Derivation of planetary topography using multi-image shape-from-shading. Planet. Space Sci. 54, 661–674.
Lorenz, R.D., 2023. Planetary landings with terrain sensing and hazard avoidance: A review. Adv. Space Res. 71, 1–15.
Lowe, D.G., 2004. Distinctive image features from scale-invariant keypoints. Int. J. Comput. Vis. 60, 91–110.
McEwen, A.S., 1991. Photometric functions for photoclinometry and other applications. Icarus 92, 298–311.
McEwen, A.S., 1996. A precise lunar photometric function. Lunar Planet. Sci. 27, 841.
McEwen, A.S., Eliason, E.M., Bergstrom, J.W., et al., 2007. Mars Reconnaissance Orbiter's High Resolution Imaging Science Experiment (HiRISE). J. Geophys. Res. 112, E05S02.
McGuire, P.C., Wolff, M.J., Smith, M.D., et al., 2008. MRO/CRISM retrieval of surface lambert albedos for multispectral mapping of Mars with DISORT-based radiative transfer modeling: phase 1—using historical climatology for temperatures, aerosol optical depths, and atmospheric pressures. IEEE Trans. Geosci. Remote Sensing 46, 4020–4040.
Meng, Q., Wang, D., Wang, X., et al., 2021. High resolution imaging camera (HiRIC) on China's first Mars exploration Tianwen-1 mission. Space Sci. Rev. 217, 42.
Minnaert, M., 1941. The reciprocity principle in lunar photometry. ApJ 93, 403.
Mishchenko, M.I., 2020. Comprehensive thematic T-matrix reference database: a 2017–2019 update. J. Quant. Spectrosc. Radiat. Transf. 242, 106692.
Mishchenko, M.I., Travis, L.D., 1997. Satellite retrieval of aerosol properties over the ocean using polarization as well as intensity of reflected sunlight. J. Geophys. Res. 102, 16989–17013.
Montabone, L., Forget, F., Millour, E., et al., 2015. Eight-year climatology of dust optical depth on Mars. Icarus 251, 65–95.
Neukum, G., Jaumann, R., Basilevsky, A.T., et al., 2009. HRSC: High Resolution Stereo Camera. In: Mars Express: the Scientific Investigations. SP. ESA Communication Production Office, Noordwijk, The Netherlands, pp. 15–74.
Nicodemus, F.E., Richmond, J.C., Hsia, J.J., Ginsberg, I.W., Limperis, T., 1977. Geometrical considerations and nomenclature for reflectance (No. NBS MONO 160). National Bureau of Standards, Gaithersburg, MD.
Ockert-Bell, M.E., Bell, J.F., Pollack, J.B., et al., 1997. Absorption and scattering properties of the Martian dust in the solar wavelengths. J. Geophys. Res. 102, 9039–9050.
Petrova, E.V., Hoekzema, N.M., Markiewicz, W.J., et al., 2012. Optical depth of the Martian atmosphere and surface albedo from high-resolution orbiter images. Planet. Space Sci. 60, 287–296.
Pollack, J.B., Ockert-Bell, M.E., Shepard, M.K., 1995. Viking Lander image analysis of Martian atmospheric dust. J. Geophys. Res. 100, 5235.
Rindfleisch, T., 1966. Photometric method for Lunar topography. Photogramm. Eng. 32, 262–277.
Schon, S.C., Head, J.W., Fassett, C.I., 2012. An overfilled lacustrine system and progradational delta in Jezero crater, Mars: Implications for Noachian climate. Planet. Space Sci. 67, 28–45.
Shkuratov, Y., Kaydash, V., Korokhin, V., et al., 2011. Optical measurements of the Moon as a tool to study its surface. Planet. Space Sci. 59, 1326–1371.
Smith, D.E., Zuber, M.T., Frey, H.V., Garvin, J.B., Head, J.W., Muhleman, D.O., Pettengill, G.H., Phillips, R.J., Solomon, S.C., Zwally, H.J., Banerdt, W.B., Duxbury, T.C., Golombek, M.P., Lemoine, F.G., Neumann, G.A., Rowlands, D.D., Aharonson, O., Ford, P.G., Ivanov, A.B., Johnson, C.L., McGovern, P.J., Abshire, J.B., Afzal, R.S., Sun, X., 2001. Mars Orbiter Laser Altimeter: Experiment summary after the first year of global mapping of Mars. J. Geophys. Res. 106, 23689–23722.
Smith, D.E., Zuber, M.T., Neumann, G.A., Lemoine, F.G., Mazarico, E., Torrence, M.H., McGarry, J.F., Rowlands, D.D., Head, J.W., Duxbury, T.H., Aharonson, O., Lucey, P. G., Robinson, M.S., Barnouin, O.S., Cavanaugh, J.F., Sun, X., Liiva, P., Mao, D., Smith, J.C., Bartels, A.E., 2010. Initial observations from the Lunar Orbiter Laser Altimeter (LOLA): LOLA INITIAL OBSERVATIONS. Geophys. Res. Lett. 37, L18204.
Soderblom, J., Belliii, J., Hubbard, M., et al., 2006. Martian phase function: Modeling the visible to near-infrared surface photometric function using HST-WFPC2 data. Icarus 184, 401–423.
Spiga, A., Forget, F., 2008. Fast and accurate estimation of solar irradiance on Martian slopes. Geophys. Res. Lett. 35, L15201.
Stamnes, K., Tsay, S.-C., Wiscombe, W., et al., 1988. Numerically stable algorithm for discrete-ordinate-method radiative transfer in multiple scattering and emitting layered media. Appl. Opt. 27, 2502.
Tan, X., Liu, J., Zhang, X., et al., 2021. Design and validation of the scientific data products for China's Tianwen-1 mission. Space Sci. Rev. 217, 69.
Tao, Y., Muller, J.-P., Xiong, S., Conway, S.J., 2021. MADNet 2.0: pixel-scale topography retrieval from single-view orbital imagery of Mars using deep learning. Remote Sens. (Basel) 13, 4220.
Tenthoff, M., Wohlfarth, K., Wöhler, C., 2020. High resolution digital terrain models of Mercury. Remote Sens. (Basel) 12, 3989.
Thomas, N., Markiewicz, W.J., Sablotny, R.M., et al., 1999. The color of the Martian sky and its influence on the illumination of the Martian surface. J. Geophys. Res. 104, 8795–8808.
Thomas, N., 2001. Light Scattering in the Martian Atmosphere: Effects on Surface Photometry. In: Williams, I.P., Thomas, N. (Eds.), Solar and Extra-Solar Planetary Systems, Lecture Notes in Physics. Springer Berlin Heidelberg, Berlin, Heidelberg, pp. 191-204.
Tomasko, M.G., Doose, L.R., Lemmon, M., et al., 1999. Properties of dust in the Martian atmosphere from the Imager on Mars Pathfinder. J. Geophys. Res. 104, 8987–9007.
van Diggelen, J., 1951. A photometric investigation of the slopes and heights of the ranges of hills in the Maria of the moon. Bull. Astron. Inst. Neth. 11, 283–289.
Vincendon, M., Langevin, Y., Poulet, F., et al., 2007. Recovery of surface reflectance spectra and evaluation of the optical depth of aerosols in the near-IR using a Monte Carlo approach: Application to the OMEGA observations of high-latitude regions of Mars. J. Geophys. Res. 112.
Wildey, R., 1975. Generalized photoclinometry for Mariner 9. Icarus 25, 613–626.
Wolff, M.J., Smith, M.D., Clancy, R.T., et al., 2009. Wavelength dependence of dust aerosol single scattering albedo as observed by the Compact Reconnaissance Imaging Spectrometer. J. Geophys. Res. 114, E00D04.
Woodham, R.J., 1980. Photometric method for determining surface orientation from multiple images. Opt. Eng. 19.
Wu, B., Dong, J., Wang, Y., et al., 2021a. Characterization of the candidate landing region for Tianwen-1 - China's first mission to Mars. Earth Space Sci. 8.
Wu, B., Dong, J., Wang, Y., et al., 2022. Landing Site Selection and Characterization of Tianwen-1 (Zhurong Rover) on Mars. JGR Planets 127.
Wu, B., Liu, W.C., Grumpe, A., et al., 2018. Construction of pixel-level resolution DEMs from monocular images by shape and albedo from shading constrained with low-resolution DEM. ISPRS J. Photogramm. Remote Sens. 140, 3–19.
Wu, B., Li, F., Hu, H., et al., 2020. Topographic and geomorphological mapping and analysis of the Chang'E-4 landing site on the far side of the Moon. Photogramm. Eng. Remote Sensing 86, 247–258.
Wu, B., Li, Y., Liu, W.C., et al., 2021b. Centimeter-resolution topographic modeling and fine-scale analysis of craters and rocks at the Chang'E-4 landing site. Earth Planet. Sci. Lett. 553, 116666.
Zimbelman, J.R., 2010. Transverse Aeolian Ridges on Mars: First results from HiRISE images. Geomorphology 121, 22–29.